Historical and projected changes in the Southern Hemisphere Sub-tropical Jet during winter from the CMIP5 models

SHEEBA NETTUKANDY CHENOLI*, MUHAMMAD YUNUS AHMAD MAZUKI, JOHN TURNER[1], AZIZAN ABU SAMAH

National Antarctic Research Centre, Institute of Postgraduate Studies,

University of Malaya, 50603 KUALA LUMPUR, Malaysia

[1] Permanent affiliation, British Antarctic Survey, Cambridge

* Correspondence to: Sheeba Nettukandy Chenoli, National Antarctic Research Centre, Institute of Postgraduate Studies, University of Malaya, 50603 KUALA LUMPUR, Malaysia; e-mail: sheeba@um.edu.my

ACKNOWLEDGEMENT:

This study was funded by University Malaya Research Grant (UMRG RG176-12SUS) and Ministry Of Science Technology and Innovation (Malaysia) Grant Flag Ship (GA007-2014FL). We acknowledge the World Climate Research Programme's Working Group on Coupled Modelling, which is responsible for CMIP, and we thank the climate modeling groups (listed in Table 1 of this paper) for producing and making available their model output. For CMIP the U.S. Department of Energy's Program for Climate Model Diagnosis and Intercomparison provides coordinating support and led development of software infrastructure in partnership with the Global Organization for Earth System Science Portals. The European Centre for Medium Range Weather Forecasting is thanked for providing the ERA-Interim datasets. Authors would also like to thank Mr Ooi See Hai, National Antarctic Research Center for his constructive suggestions and comments.

ABSTRACT

We present projected changes in the speed and meridional location of the Subtropical Jet (STJ) during winter using output of the Coupled Model Intercomparison Project Phase 5 (CMIP5) models. We use the ERA-Interim reanalysis dataset to evaluate the historical simulations of the STJ by 18 of the CMIP5 models for the period 1979-2012. Based on the climatology of the STJ from ERA-Interim, we selected the area of study as 70°E - 290°E and 20°S - 40°S, which is over the Indian and Southern Pacific Oceans, and 300 hPa to 100 hPa to reduce altitude-related bias. An assessment of the ability of the CMIP5 models in simulating ENSO effects on the jet stream were carried out using standardized zonal wind anomalies at 300 hPa to 100 hPa. Results show that 47% of the CMIP5 models used in this study were able to simulate ENSO impacts realistically. In addition, it is more difficult for the models to reproduce the observed intensity of ENSO impacts than the patterns. The historical simulations of the CMIP5 models show a wide range of trends in meridional movement and jet strength, with a multi-model mean of 0.04°decade^{-1} equatorward and 0.42 ms^{-1}decade^{-1} respectively. In contrast to the ERA-Interim analysis, 94% of the CMIP5 models show a strengthening of the jet in the historical runs. Variability of the jet strength is significantly (5%) linked to the sea surface temperature changes over the eastern tropical Pacific. The CMIP5 model projections with Representative Concentration Pathways (RCPs) 4.5 and 8.5 were used for analysis of changes of the STJ for the period 2011-2099. Based on the RCP 4.5 (RCP 8.5) scenario the multi-model mean trend of the 18 CMIP5 models project a statistically significant (5% level) increase in jet strength by the end of the century of 0.29 ms^{-1}decade^{-1} (0.60 ms^{-1}decade^{-1}). Also, the mean meridional location of the jet is projected to shift poleward by 0.006°decade^{-1} (0.042° decade^{-1}) in 2099 during winter, with the only significant (5%) trend being with RCP 8.5.

1.0 Introduction

The Subtropical Jet Stream (STJ) has an important role in the climate of the Southern Hemisphere (SH), influencing the storm tracks, surface cyclogenesis, precipitation, and oceanic conditions. Jet streams are important because their position signifies the existence of strong baroclinicity. They play a major role in the formation and development of mid-latitudes cyclones (Holton, 2004) with the jet entrance and exit regions have been linked dynamically to surface cyclogenesis and anticyclogenesis respectively. Jet streams also affect air transport because of the clear-air turbulence associated with the jet cores (Bluestein, 1993). In addition, the high wind speeds associated with jet cores can transport pollutants over large distances in short time periods, and the strong lateral and vertical wind shears enable strong dispersion of localised pollutants (Koch et al, 2006). A recent study by Rudeva and Simmonds (2015) also investigated the variability and trends in the frontal activity as a key component for understanding climate variability. Therefore changes in jet stream location, intensity, or altitude can have important consequences for the SH climate. The structure of the upper tropospheric jets shows large differences between the two hemispheres, largely as a result of the different land-sea distributions. In the Northern Hemisphere (NH), the Polar Front Jet (PFJ) is a year-round feature from the southeast USA, across the Atlantic Ocean and into Europe, with the jet being stronger during the winter season. The STJ extends from North Africa across Asia, before linking with the strong PFJ south of Japan and extending across the Pacific (Bals-Elsholz et al, 2001; Archer and Caldeira, 2008). In contrast, the limited high orography and extensive ocean areas of the SH result in a more zonally symmetric structure to the jet, but with a greater seasonal variability because of the larger Equator to Pole temperature difference. The strongest wind speeds are associated with the STJ in winter ((June, July and August (JJA)) (Lee and Kim, 2003; Nakamura et al, 2004; Koch et al, 2006; Archer and Caldeira, 2008; Pena-Ortiz et al, 2013) when it rings most of the hemisphere, but with the highest speeds being across Australia and the western south Pacific Ocean. The PFJ is strongest over the autumn to spring seasons, with the highest speeds across the Atlantic and Indian Oceans. Many studies have shown that the SH jets exhibit a concentric structure, with a persistent branch around Antarctica and a seasonally varying branch at about 30°S (Chen et al, 1996). A feature of the SH jet structure is the 'split jet' across New Zealand (Bals-Elsholz et al, 2001) between the STJ near 30°S and the PFJ near 50°S. The equatorward branch of the jet is the STJ, which is located between 25°S and 30°S from the central South Indian Ocean across Australia to the east-central South Pacific Ocean (Bals-Elsholz et al, 2001). The poleward branch of the time-mean split jet is the PFJ. As noted earlier, the STJ is not a permanent continuous structure; rather it is fragmented and meandering with notable wind speed and elevation variations. Therefore, defining the jet stream boundaries presents some difficulties.

A number of recent studies (Lu et al, 2007, Kang and Lu, 2012, Liu et al, 2012, Min and Son 2013) have indicated substantial interest in the expansion of the Hadley Circulation (HC) associated with a poleward movement of the jet streams. Figure 1 shows the approximate boundary between the HC and STJ for July 1997 between 240-260°E. The area and month were selected in order to show HC and STJ core clearly. The rectangular box indicates the area where the STJ location coincide with the poleward edge HC boundary. Figure 1 provides a visualization of how the expansion/contraction of the HC influences the location of the STJ.

Recent observational (Seidel et al, 2008; Davis and Rosenlof, 2012) and modeling studies (Lu et al, 2007, 2009; Son et al, 2009, 2010; McLandress et al, 2011; Polvani et al, 2011a; Ming and Ramaswamy, 2011) show that the tropical belt has been expanding polewards in both hemispheres due to increases in the concentration of greenhouse gases. Thus, further investigation is needed to better understand the HC change in the past and future climate as concluded by Min and Son (2013).

The strength of the STJ is strongly affected by the state of the sea surface temperatures (SST) across the tropical ocean in response to the changes in phase of the El Niño Southern Oscillation (ENSO) (Sampe et al, 2010). The ENSO influence is noticeable more in the Pacific sector than the other parts of the SH (Turner, 2004; Gallego et al, 2005). The effect of the ENSO cycle on the jet stream is noticeable in the meridional location of the STJ and in particular on its strength. During El Niño phase the strength of the STJ over the Pacific area is 25-50% greater than that during the La Niña phase (Gallego et al, 2005). In contrast, the STJ speed over the Atlantic and Indian Oceans shows a decrease of 10–20% during the El Niño phase (Gallego et al, 2005). Furthermore, the location of the STJ over the Pacific area is found to be displaced northward compared to the mean location. It should be noted that Gallego et al (2005) used an objective algorithm for detecting and tracking the jet based on the geostrophic streamline of maximum average velocity. Therefore, there can be some differences between their finding and this study, since we use a different approach to locate the STJ.

In this paper we examine how the models of the Coupled Model Intercomparison Project Phase 5 (CMIP5) exercise represent the STJ for the recent past and consider changes in the jet location and strength over the 21st Century under conditions of increasing greenhouse gas concentrations and recovery of the ozone hole. The aims are to quantify the trends in the strength and meridional location of the SH STJ since 1979, to assess the ability of the CMIP5 models to reproduce the recent variability of the STJ, and to determine the role of ENSO on the variability of the jet. We also examine projections of changes in the STJ over the 21st Century from the models. In Section 2, we describe the data used and the methodology. In Section 3, we present the climatology of the STJ, examine the role of broad scale phenomena on the variability of the jet stream and present an analysis of the trends in the jet strength and position based on ERA-Interim analyses as well as the CMIP5 models. The section also provides STJ variability under Representative Concentration Pathways (RCP) 4.5 and 8.5 projections. Finally, a discussion is presented in Section 4, with Section 5 consisting the results and conclusions.

2.0 Data and Methodology

Here we have used output from 18 of the CMIP5 models. This number of models were used in order to make the study computationally affordable and also the models were selected to ensure that all the required parameters are available for both future scenarios. We used 'historical' (all forcing) output for simulations covering the period 1979-2012. We used this period so that the model output could be compared with that from ERA-Interim. For the projections over the 21st Century (2011 - 2099) we used runs based on the RCPs 4.5 and 8.5. RCP 4.5 is a scenario of an increase in global mean radiative forcing relative to the year 1750 of 4.5 Wm^{-2}, with carbon emission peaking in 2040 and stabilizing by 2100. RCP 4.5 is an intermediate energy use scenario, while RCP 8.5 is a high energy-intensive scenario, which is the result of high population growth and lower rate of technology development (van Vuuren et al, 2011).

In assessing the performance of the CMIP5 models in simulating the location and speed of the STJ, we compared the model output with the ERA-Interim reanalysis fields ((Dee et al, 2011), which are regarded as the most realistic of the various reanalysis datasets (Bromwich et al, 2011; Bracegirdle and Marshall, 2012; Simmons et al, 2014). We used data for the period 1979 – 2012 because the quality of the fields is questionable at high southern latitudes prior to 1979 due to the lack of satellite sounder data for use in the data assimilation process. To assess the impacts of changes in SST on the jet strength, Hadley Centre Sea Ice and Sea Surface Temperature data (HadISST) (Rayner et al, 2003) has been used.

In order to select the area of study, we developed a climatology of the STJ from ERA-Interim based on the zonal wind at 300 hPa-100 hPa. The monthly and seasonal mean zonal wind component, and the annual cycle of wind speed as well as the location of the jet stream were analysed to determine the best area to use. Here we examine the year-to-year features of the STJ during winter in order to distinguish it from the PFJ. Analysis of the variations in the strength of the STJ and its meridional position shows that the spatial location of the jet core is always confined to the area 20°S to 40°S, 70°E - 290°E during winter and the study area selected shows a clearly defined jet stream. This is to separate the core of the STJ from the PFJ and to avoid the Atlantic sector where the STJ merges with the PFJ. In addition, several earlier studies (Rind et al, 2001; Liu et al, 2002; Yuan 2004) showed that the ENSO-related changes in the strength of the STJ are mainly located in this area. Furthermore, teleconnections, are commonly strongest in winter when the mean meridional temperature gradient is large (Strong and Davis, 2008). Based on this we have selected the area defined above as our study area (Figure 2), which covers parts of the Indian Ocean and the Southern Pacific Ocean.

We used three-dimensional analysis similar to that adapted by Pena-Ortiz et al. (2013) to quantify the strength and position of the STJ. Usually, analysis of jet streams is carried out on a selected pressure level i.e. 200 hPa (Athanasiadis et al, 2010). However, in our study, depending on the location and season, the jet core of STJ is not always found at 200 hPa. Thus, a three-dimensional analysis helps to reduce the bias related to altitude position (Strong and Davis 2008, Manney et al, 2011). In this method, in order to identify the jet core, the monthly zonal winds are analysed to locate the zonal wind maximum in the vertical between 300 and 100 hPa and latitude from 20°S to 40°S at each longitudinal slice between 70°E - 290°E. The wind maximum that exceeds 30 ms^{-1} is used to identify the jet core. The latitude of this wind maximum is taken as the meridional location of the jet stream and the magnitude of wind maximum as the jet strength. The resultant data were then visually checked to filter any wind maxima that were not continuous in strength and latitudinal position for that particular month. To obtain the mean strength and location for the particular month, the jet core values and the corresponding latitudes from all the longitudinal slices were averaged. The procedure is repeated for JJA for the historical period 1979-2012 and during the future projection period 2011-2099 for all the selected CMIP5 models. When taking the multi-model mean of 18 models selected for the study, we use the unweighted mean which gives equal weight to all the models. This is based on the assumption that individual model biases will be partially canceled and the multi-model average prediction will be more likely to be correct than a prediction from a single model (Knutti et al, 2010). Wenzel et al. (2016) attempted to investigate whether the unweighted multi-model mean of CMIP5 models can be improved by applying a process-oriented multiple diagnostic ensemble regression in analyzing austral jet position. They found that the weighted multi-model mean does not substantially differ from the equal weighted mean in simulating the long term jet positon; however, it merely reduces the uncertainty in the ensemble mean projection.

3.0 Climatology of the STJ

3.1 Annual Cycle

Based on the long-term monthly average of zonal wind (1979 to 2012) it can be seen clearly that (Figures 3(a) and (b)) the strength as well as the location vary strongly over the seasons. The STJ is strongest during the winter months (JJA) and weakest in summer (December, January and February (DJF)), with a large interannual variability in strength. During winter and summer the average zonal wind speeds of STJ are 49.43 ms^{-1} and 25.87 ms^{-1} respectively with interannual standard deviations of 3.56 ms^{-1} and 4.68 ms^{-1} respectively. The STJ during summer displays a maximum poleward location at 31°S and shifts equatorwards during autumn and spring. During winter the meridional location of STJ is more stable at around 30°S.

3.2 Seasonal cycle

The seasonal mean zonal wind speeds from ERA Interim between 300-100 hPa are illustrated in Figure 4. The STJ is strongest (core speed >45 ms^{-1}) and most prominent during JJA (Figure 4 (a)) and it merges with the PFJ forming a concentric ring structure around Antarctic. The core of zonal wind maximum of the STJ is located at 30°S between the longitudes 70°E to 240°E. During spring (SON) the pattern remains similar to that in JJA with a lower maximum zonal wind speed of 40 ms^{-1} and a location one degree equatorwards within the same longitudinal band as JJA. The STJ is, however, not well defined during summer. During SON, the STJ and PFJ are distinguishable and the location of the STJ is similar to its winter position. Therefore, it is clear that, in all seasons, the STJ is confined to the area 70°E to 240°E and latitude from 20°S to 40°S.

4.0 The impact of ENSO on the speed and location of the STJ

ENSO is the dominant factor of global climate variability on inter-annual to decadal time scales. It originates in the tropical eastern Pacific region and modulates (Zhang et al, 1997; Trenberth, 1997) the latitudinal position and strength of the STJ (Chen et al, 1996; Gallego et al, 2005). The influence of ENSO on the SH upper-level winds, especially on the variability of the wind strengths has been recognized for some time (Chen et al, 1996; Sinclair, 1996). An accurate ENSO simulation in the climate models poses a difficult task since it involves complex interactions of various oceanic and atmospheric processes. Nevertheless, the ability of climate models to simulate ENSO has improved over the recent few years (Leloup et al, 2008; Bellenger et al, 2013, Watterson, 2015). As noted by Bellenger et al (2013), even though there is no significant improvement in the CMIP5 models performance in simulating ENSO when compared to the CMIP3, certain features and processes of ENSO life cycle, such as the location of surface temperature anomalies and seasonal phase locking, have been improved slightly. It should be noted that ENSO is a natural mode of climate variability and that while the ‘historical’ runs of the CMIP5 models will simulate tropical Pacific climate variability on ENSO timescales, individual El Niño and La Niña events will not occur at the same times as those in the ‘real’ world. This is discussed further in the following sections.

A previous study (Leloup et al, 2008) has shown that there is a large variation in the spatial pattern and magnitude of SST in the equatorial Pacific during ENSO as simulated by the

CMIP3 models when compared to the observations. The CMIP3 models do not systematically simulate their maximum ENSO amplitude in the same area as observed (Guilyardi, 2006; Achuta Rao and Sperber, 2006; Leloup et al, 2008) and the spatial patterns extend too far into the western Pacific. In order to identify El Niño and La Niña years in the CMIP5 models and ERA-Interim reanalysis, we use SST anomalies along the equatorial Pacific as defined by Leloup et al (2008). SST is averaged over the region 5°N-5°S, 150°E-280°E each month from January 1979 to December 2012. Monthly SST anomalies for each model were calculated and SST anomalies were then smoothed using a 3 month running mean. With this approach, El Niño (La Niña) years are defined as years with at least six consecutive months with SST anomaly greater (lower) than half a standard deviation of the SST anomalies (Leloup et al, 2008) for each model. All the El Niño years and La Niña years within 1979 to 2012 were used to study the impact of ENSO on the jet stream. Average winter anomalies of 300-100 hPa zonal wind speed of all El Niño and La Niña years are then computed separately and compared with zonal wind speeds anomaly from ERA-Interim reanalysis to assess how the CMIP5 models simulated the impacts of ENSO on the jet stream.

Figures 5 (a) and 5 (c) show the average zonal wind speed and Figure 5 (b) and 5 (d), the associated standardised anomalies (anomalies of zonal wind divided by standard deviation of zonal wind at each grid point) in JJA for the period 1979-2012 for El Niño years (nine events) and La Niña years (seven events) respectively. These were derived from HadISST data based on the method by Leloup et al (2008). Standardised zonal wind anomalies during El Niño years show a strong positive zonal wind standardised anomaly of 0.80 over the southern Pacific Ocean between Australia and South America, (Figure 5(b)) while a negative zonal wind speed anomaly centred at 25°S is noted over the Atlantic Ocean and south of Africa. During El Niño events, there is strengthening of the STJ and weakening of the PFJ. It is evident from the standardised anomalies (Figure 5(b) and 5(d)) of average zonal wind that during El Niño and La Niña events, the STJ and PFJ show an oscillation in the strength over the Pacific Ocean. The STJ is stronger with a maximum standardised wind anomaly of 0.8 and shifts eastward in the Pacific Ocean during the El Niño phase. It is weaker during La Niña events with a negative standardised anomaly of 0.8. Bals-Elsholz et al. (2001) suggest that a baroclinic zone across Australia develops during the austral winter as a result of the cooling of the continent in contrast to the western Pacific warm pool during El Niño. Hence, this modulates the strength and position of the STJ (Seager et al, 2003).

Standardised zonal wind anomalies from the 18 CMIP5 models (see Table 1 for the number of El Niño and La Niña years) are shown in Figure 6 and Figure 7. Four models CCSM4, NorESM1-M, MPI-ESM-LR, and HadCM3 (Figure 6 (a)-(d)) and CCSM4, NorESM1-M, CanESM2, and HadCM3 (Figure 7 (a)-(d)) were able to capture the features of the El Niño and La Niña impacts on the STJ close to the observed patterns both in terms of the locations as well as the changes in the strength. Other models, namely CNRM-CM5, CSIRO-MK 3.6.0, CanESM2, and GFDL-CM3 show slight deviations from the observed El Niño pattern. These models (Figure 6 (e)-(h)) have an El Niño impact pattern similar to ERA-Interim reanalysis with slight differences in terms of magnitude and pattern. Among them, CanESM2 was able to capture the observed El Niño and La Niña patterns well. During La Niña years, the models MPI-ESM-LR, GFDL-CM3, IPSL-CM5A-MR, and IPSL-CM5A-LR (Figure 7 (e)-(h) were able to reproduce the spatial pattern of average zonal wind anomaly with slight variations. Apart from the above, INMCM4, IPSL-CM5A-LR, BCC-CSM1-1, HadGEM2-CC and MIROC5, 33% of the 18 models and four models CNRM-CM5, HadGEM2-CC, INMCM4, MIROC5 fail to reproduce the observed pattern of El Niño and La Niña impacts on the jet stream respectively. As noted by Bellenger et al. (2013), the CNRM-CM5 and CCSM4 models are some of the CMIP5 models that have best ENSO characteristics and these models are more reliable to study ENSO dynamics and its sensitivity to external forcing.

Anomaly correlation coefficient (ACC) of zonal wind for all the El Niño and La Niña events from the CMIP5 models with ERA Interim reanalysis are calculated in order to quantify the ability of CMIP5 model to simulate ENSO impacts on STJ (Figure 8 and Figure 9). The area shaded red indicates the values from each individual model are positively correlated with the ERA Interim. The opposite is true for blue shaded area.

In order to better characterise the representation of the magnitude of the impact of ENSO on the jet stream in CMIP5 models and ERA-Interim in the study area, the ACC average in the study area are calculated (Figures 10 (a) and (b)). The whiskers in the figures indicate the 95% confidence interval. The models CanESM2, CSIRO-MK3-6-0, NorESM1-M, GFDL-CM3, HadCM3 and HadGEM2-ES reveal a moderate correlation (0.40-0.60) of El Niño impact on the jet stream between CMIP5 models and ERA-Interim in the study area. For La Niña impacts 55% of the CMIP5 models show a higher ACC (0.45-0.75). In general, moderate to higher ACC averages from CanESM2, CSIRO-MK3-6-0, NorESM1-M, GFDL-CM3, HadCM3 indicate that they display relatively good El Niño and La Niña characteristics in terms of magnitude and location. A recent paper by Molteni et al (2015) provides a critical insight into the understanding of modeling extratropical teleconnection with the Indo-Pacific region. They stated that AGCM coupled model reproduces the broad features of tropical and extra-tropical teleconnections with a good degree of fidelity. However, the traditional method of linearly relating circulation anomalies to SST anomalies is only appropriate for signals originated in the central and east Pacific and it fails to identify the response to anomalous heating over the west Pacific and most of the Indian Ocean. They concluded that accurate simulation of inter-decadal variability of SST is crucial in reproducing the teleconnection relationship. Also, particular care must be taken in interpreting the results of the AGCM simulation that are based on the SST because of the absence of feedback between convection and SST over the warm pool region.

5.0 The representation of the STJ in the historical runs of the CMIP5 models

Figure 11 (a) shows the trend in the jet strength in ERA-Interim and all the CMIP5 models used in this study. The dotted vertical line and the dotted-dash lines in the figure represent the trend in the jet strength in ERA-Interim and position of zero respectively. The blue coloured data points show models that have statistically significant trends in the strength at the 5% significant level using two-tailed student test with reduced degree of freedom (Bretherton et al, 1999). ERA-Interim and HadGEM2-CC show a negative trend in the jet strength, but the trends are not significant. Five models, GFDL-CM3, HadGEM2-ES, CanESM2, GISS-E2-R and CSIRO-MK3.6.0 show a significant positive trend in the jet strength. The trend in the jet strength based on ERA-Interim is -0.176 ms^{-1} $decade^{-1}$, whereas the multi-model mean of all 18 CMIP5 shows a strengthening of 0.421 ms^{-1} $decade^{-1}$ (Figure 11(b)). Figure 11(b) shows that the ERA-Interim displays a strong interannual variability in the STJ strength compared to the multi-model mean. Compared to ERA-Interim, the 18 models have large differences in their interannual variability. The models CCSM4, CNRM-CM5, CSIRO-MK3-6-0, GFDL-CM3, GISS-E2-R, HadCM3 and HadGEM2-CC shows standard deviations (1.88 ms^{-1} to 2.42 ms^{-1}) comparable to ERA-Interim (2.38 ms^{-1}) where as HadGEM2-ES, INMCM4, IPSL-CM5A-LR, IPSL-CM5A-MR, MICROC-5, MICROC-ESM, MICROC-ESM-CHEM, MPI-ESM-LR and NorESM1-M show lower standard deviation in the STJ strength compared to ERA-Interim.

Figures 12 (a) and (b) show the spatial trend in the 300-100 hPa zonal wind speed from 1979-2012 as represented in ERA-Interim and the multi-model average respectively in the study area. Examination of the trend in SST over the tropical Pacific from HadISST (Figure 13 (a)) shows a slight negative trend. This is in agreement with the recent La Niña-like trend revealed in the tropical SST (Zhang et al, 2011) and even in the SST pattern in the sub-surface ocean from different reanalysis data sets (Ishii et al, 2006; Carton and Giese, 2008). On the other hand, the SST trend in the multi-model mean demonstrates (Figure 13 (b)) an El Niño like pattern in the tropical SSTs is consistent with the strengthening of the jet. In order to establish the link between the trend in the strength of the STJ and tropical SSTs we relate the trend in the winter strength of the STJ with the trend in SSTs in the Niño 3.4 region from 1979 to 2012. Figure 14 shows the variation of tropical SSTs in the Niño 3.4 region and the strength of the STJ and indicates that there is a significant (5%) correlation of 0.66.

The mean meridional location of the STJ in the ERA reanalysis is at 29.7°S (Figure 15 (a)). The ERA data indicates that there has been a poleward shift in the location of the STJ (Figure 15 (b)), while some of the CMIP5 models show an equatorward shift of the STJ. Figure 16 shows the time series of the jet position from ERA-Interim and the multi-model mean. The CMIP5 multi-model mean obviously does not have the three equatorward migrations corresponding to the three strong El Niño events in 1982/83, 1986/87, and 1997/98 since the models will have their El Nino events at different times. During the El Nino events, contraction of the Hadley cell leads to the equatorward shift of the STJ (Lu et al 2008). Time series of jet locations from individual models (not shown here) show that the 50% of models used for the study fail to reproduce these equatorial shift during strong El Niño events in the individual models defined on the basis of model SST (refer section 4.0). The multi-model mean shows a poleward shift of the STJ at a rate of 0.036°decade^{-1} whereas 0.100°decade^{-1} is observed in ERA-Interim during the period 1979-2012 (Figure 16). Several recent studies (Polvani et al, 2011 b, Lee and Feldstein, 2013) associate the recent poleward shift of the STJ with a cooling of the lower stratospheric polar cap caused by stratospheric ozone depletion. They suggest that high latitude cooling due to ozone depletion increases the meridional temperature gradient between the polar region and the extratropics, leading to the poleward shift of the westerly winds. The poleward jet shift shows large seasonal variations, with a comparatively large shift during the summer and autumn seasons and insignificant shifts during winter and spring (Lee and Feldstein, 2013). It can also be related to the trend in the Southern Annular Mode (SAM) index during different seasons. A recent paper by Simmonds (2015) shows that there is a significant positive trend in SAM index during the Southern Hemisphere summer and autumn and no significant trends are detected in either JJA or spring (SON) during the period 1979-2013.

6.0 Future trends in the strength and location of the STJ and the relationship with SSTs

Examination of the CMIP5 model zonal winds over the period 2011 to 2099 shows that the speed of the STJ is predicted to strengthen significantly under both RCP 4.5 (82 % of the models) and RCP 8.5 (94 %) scenarios (Figure 17 (a) and 17 (b)). The multi-model average suggests a significant increase in the jet strength of 0.292 ms^{-1} decade^{-1} for RCP 4.5 and 0.604 ms^{-1} decade^{-1} for RCP 8.5. The trend in the jet strength from the multi-model mean from RCP 4.5 is approximately double that from the RCP 8.5 (Figure 18). Also, the speed of the STJ after 2050 shows a large divergence between the two scenarios RCP 4.5 and RCP 8.5. The large difference in the strengthening of STJ in RCP 4.5 and RCP 8.5 is due to the fact that the RCP 4.5 scenario shows little change during the period of stratospheric ozone recovery (2050), whereas there is a significant change in the speed of the STJ in RCP 8.5 scenario due to the exponential increase in greenhouse gas concentrations. Gerber and Son (2013) also suggest that differences in ozone-related polar stratospheric temperatures would be able to explain the divergence of future jet trends better than that compared to the temperature differences due to global warming in the CMIP5 models.

Figures 19 (a) and (b) show the trend in the meridional locations of the STJ for RCPs 4.5 and 8.5. All the models show a poleward shift under these two scenarios. However, in most of the models with RCP 4.5, the changes are small and insignificant, while in RCP 8.5, 47% of the models shows a significant (at 5% confidence level) poleward shift. The ensemble mean shift of the jet latitude is shown in Figure 20. RCP 4.5 results in little change in the mean position of the jet and the shift by the end of the century is 0.006° decade^{-1} and 0.042° decade^{-1} towards the pole in RCP 4.5 and RCP 8.5 respectively.

6.1 Inter-model variability in the future projections of the STJ linked to SSTs in the individual models

As would be expected, there is a strong correlation with most of CMIP5 models between projected changes in the strength of the STJ and changes in the SSTs in the Niño 3.4 region. Figure 21 shows the correlation between the multi-model mean projected jet strength (2011-2099) with the projected multi-model mean of SST. For both scenarios there is a strong correlation between SST and jet strength, in particular near the equatorial Pacific.

Figure 17 (a) shows that there are large differences in the projected magnitude of strength of the STJ from the CMIP5 models with the 4.5 scenario. To investigate the causes of the large spread in the projected jet strength, the possible role of SSTs in the CMIP5 models was assessed. For the RCP 4.5 scenario, IPSL-CM5A-MR and INM-CM4 show the lowest and CSIRO-MK3.6.0 and MIROC-ESM-CHEM the highest significant trend in the jet strength (Figure 17 (a)). Figure 22 (a),(b),(c) and (d) show the projection of SST trend from the models IPSL-CM5A-MR and INM-CM4 and CSIRO-MK3.6.0 and MIROC-ESM-CHEM. Comparing the SST trends, it is evident that the models with low trend in the strength have the lowest SST trend in the Niño 3.4 region, which suggests that the inter-model variability in the magnitude of the jet strength is linked to the SSTs predicted by the individual models.

7.0 Discussion and Conclusions

In this study historical simulations and future projections of the STJ using 18 CMIP5 models were evaluated. Based on the climatology, the area of study was defined as 20°S to 40°S, 70°E to 290°E which covers part of the Indian Ocean and Southern Pacific Ocean and the levels selected were from 300 hPa to 100 hPa. Standardised zonal wind speed wind anomalies at 200 hPa were used to investigate the impacts of ENSO on the strength of the STJ. A study of ENSO effects on the jet stream was carried out to assess the impacts of the cycle on the jet stream and to assess the ability of the CMIP5 models in simulating ENSO. We have shown that 47% of the CMIP5 models used in this study were able to simulate ENSO impacts realistically. Furthermore, it is more difficult for the models to reproduce the observed intensity of ENSO impacts than the pattern. It is also clear that there are differences in the responses of the models in simulating the impacts of El Niño and La Niña on jet streams.

The ERA-Interim reanalysis shows long term mean wind strength of the STJ of 40 ms^{-1} with the jet position close to 29.7°S. With regard to the historical trend in the strength of the STJ, ERA interim shows a trend of -0.18 ms^{-1} $decade^{-1}$ whereas the multi-model mean of all 18 CMIP5 shows a strengthening of 0.42 ms^{-1} $decade^{-1}$. To investigate the causes of the differences in trends in the models and observation, the possible role of SST in the CMIP5 models was assessed. The analysis showed that there is a significant correlation (correlation coefficient 0.66) between the tropical SSTs across the Niño 3.4 region and the trend in the strength of the STJ. The trend in the meridional location of the STJ based on ERA-Interim shows that the STJ has negligible latitudinal shift during the austral winter. This is due to the fact that the SST in the Niño 3.4 shows a slight negative trend during the period of study contributing to an insignificant shift. As shown by Thompson and Solomon (2002) and Polvani et al (2011 b), the poleward jet shift is largely caused by the changes in the stratospheric ozone concentration and the contribution due to the increase in the greenhouse gases is comparatively smaller. Though the ozone depletion occurs in October to November the tropospheric response is strongest during summer.

The projected changes in the strength and meridional location documented in this study show a wide range of responses among the different models. The RCP 4.5 (RCP 8.5) projection suggests an increase in the jet strength speed of up to 2.5 ms^{-1} (5.5 ms^{-1}) by the end of the century for 64.7% (82.2%) of the models. The jet latitude under RCP 4.5 (RCP 8.5) is projected to move poleward by 0.06° (0.4°) with 11.8% (52.9%) of the models showing significant poleward shift. There are large differences in the projected magnitude of the trend in the STJ strength in individual CMIP5 models. We have shown that the inter-model variability in the projection of the strength of STJ is well correlated with biases in the equatorial SSTs in the individual CMIP5 models.

As mentioned in the earlier part of this paper, several recent studies show that changes in STJ position are related to changes in the precipitation patterns, Antarctic sea ice extent etc. Recent positive trend in SAM also signifies the polewards shift in the surface westerlies related to global warming. Pezza et al (2007) noted a possible link between Pacific decadal oscillation (PDO) and extratropical circulation over the Southern Ocean. Their study shows that more intense (and fewer) cyclones and anticyclones are observed during the positive PDO. In addition, Pezza et al (2008, 2012) explored the association between SH cyclones and anticyclones and the ENSO, SAM, Antarctic sea ice extent (SIE), and rainfall in southern Australia. The results indicate that there is a contraction of sea ice accompanied by the southward shift of high latitude cyclone, resulting in decreasing rainfall trend in southern Australia. This suggests that the complex interactions among the key climate features can be thought of as an interconnected SAM/SIE mechanism. Hence, realistic predictions of trends in the position of STJ and understanding the mechanisms behind such trends are very important.

REFERENCES

AchutaRao K, Sperber KR (2006) ENSO simulation in coupled ocean-atmosphere models: Are the current models better? Clim Dyn 27:1–15

Archer CL, Caldeira K (2008) Historical trends in the jet streams. Geophys. Res. Lett. 35:L08803 doi: 10.1029/2008GL033614

Athanasiadis P, Wallace JM, Wettstein JJ (2010) Patterns of Wintertime Jet Stream Variability and Their Relation to the Storm Tracks*. J. Atmos. Sci. 67: 1361-1382 doi: 10.1175/2009jas3270.1.

Bals-Elsholz TM, Atallah EH, Bosart LF, Wasula TA, Cempa MJ, Lupo AR (2001) The wintertime southern hemisphere split jet: Structure, variability, and evolution. J Clim 14:4191–4215. doi: 10.1175/1520-0442(2001)014<4191:TWSHSJ>2.0.CO;2

Bellenger H, Guilyardi E, Leloup J, Lengaigne M, Vialard J (2013) ENSO representation in climate models: From CMIP3 to CMIP5. Clim Dyn 42:1999–2018. doi: 10.1007/s00382-013-1783-z

Bluestein HB (1993) Synoptic-dynamic meteorology in midlatitudes: Volume II: Observations and theory of weather systems. Oxford University Press, USA

Bracegirdle TJ, Marshall GJ (2012) The reliability of Antarctic tropospheric pressure and temperature in the latest global reanalyses. J Clim 25:7138–7146. doi: 10.1175/JCLI-D-11-00685.1

Bretherton CS, Widmann M, Dymnikov VP, Wallace JM, Bladé I (1999) The effective number of spatial degrees of freedom of a time-varying field. J Clim 12:1990–2009. doi: 10.1175/1520-0442(1999)012<1990:TENOSD>2.0.CO;2

Bromwich DH, Nicolas JP, Monaghan AJ (2011) An assessment of precipitation changes over Antarctica and the Southern Ocean since 1989 in contemporary global reanalyses. J Clim 24:4189–4209. doi: 10.1175/2011JCLI4074.1

Carton JA, Giese BS (2008) A reanalysis of ocean climate using Simple Ocean Data Assimilation (SODA). Mon Weather Rev 136:2999–3017. doi: 10.1175/2007MWR1978.1

Chen B, Smith SR, Bromwich DH (1996) Evolution of the tropospheric split jet over the South Pacific Ocean during the 1986–89 ENSO Cycle. Mon Weather Rev 124:1711–1731

Davis SM, Rosenlof KH (2012) A multidiagnostic intercomparison of tropical-width time series using reanalyses and satellite observations. J Clim 25:1061–1078. doi: 10.1175/JCLI-D-11-00127.1

Dee DP, Uppala SM, Simmons AJ, Berrisford P, Poli P, Kobayashi S, Andrae U, Balmaseda MA, Balsamo G, Bauer P, Bechtold P, Beljaars ACM, Berg L van de, Bidlot J, Bormann N, Delsol C, Dragani R, Fuentes M, Geer AJ, Haimberger L, Healy SB, Hersbach H, Hólm EV, Isaksen L, Kållberg P, Köhler M, Martricardi M, McNally AP, Monge-Sanz BM, Morcrette J-J, Park B-K, Peubey C, de Rosnay P, Tavolato C, Thépaut J-N, Vitart F (2011)

The ERA-Interim reanalysis: configuration and performance of the data assimilation system. Q J R Meteorol Soc 137:553–597. doi: 10.1002/qj.828

Gallego D, Ribera P, Garcia-Herrera R, Hernandez E, Gimeno L (2005) A new look for the Southern Hemisphere jet stream. Clim Dyn 24:607–621. doi: 10.1007/s00382-005-0006-7

Gerber EP, Son S-W (2014) Quantifying the summertime response of the austral jet stream and Hadley cell to stratospheric ozone and greenhouse gases. J Clim 27:5538–5559. doi: 10.1175/JCLI-D-13-00539.1

Guilyardi E (2006) El Niño-mean state - seasonal cycle interactions in a multi-model ensemble. Climate Dyn 26:329–348. doi: 10.1007/s00382-005-0084-6

Holton JR (2004) An Introduction to Dynamic Meteorology, Fourth Edi. Elsevier Academic Press, California

Ishii M, Kimoto M, Sakamoto K, Iwasaki SI (2006) Steric sea level changes estimated from historical ocean subsurface temperature and salinity analyses. J Oceanogr 62:155–170. doi: 10.1007/s10872-006-0041-y

Kang SM, Polvani LM, Fyfe JC, Sigmond M (2011) Impact of polar ozone depletion on subtropical precipitation. Science 332:951–4. doi: 10.1126/science.1202131

Kang SM, Lu J (2012) Expansion of the Hadley cell under global warming: Winter versus summer. J Clim 25:8387–8393. doi: 10.1175/JCLI-D-12-00323.1

Koch P, Wernli H, Davies HC (2006) An event-based jet-stream climatology and typology. Int J Climatol 26:283–301. doi: 10.1002/joc.1255

Lee S, Feldstein SB (2013) Detecting ozone- and greenhouse gas-driven wind trends with observational data. Science 339:563–7. doi: 10.1126/science.1225154

Lee S, Kim H (2003) The dynamical relationship between subtropical and eddy-driven jets. J Atmos Sci 60:1490–1503

Leloup J, Lengaigne M, Boulanger JP (2008) Twentieth century ENSO characteristics in the IPCC database. Clim Dyn 30:277–291. doi: 10.1007/s00382-007-0284-3

Liu J, Yuan X, Rind D, Martinson DG, Nin E (2002) Mechanism study of the ENSO and southern high latitude climate teleconnections. Geophys Res Lett 29:8–11

Liu J, Song M, Hu Y, Ren X (2012) Changes in the strength and width of the Hadley circulation since 1871. Clim Past 8:1169–1175. doi: 10.5194/cp-8-1169-2012

Lu J, Vecchi GA, Reichler T (2007) Expansion of the Hadley cell under global warming. Geophys Res Lett 34:2–6. doi: 10.1029/2006GL028443

Lu J, Chen G, Frierson DMW (2008) Response of the Zonal Mean Atmospheric Circulation to El Niño versus Global Warming. J Clim 21:5835‑5851. doi: 10.1175/2008JCLI2200.1

Lu J, Deser C, Reichler T (2009) Cause of the widening of the tropical belt since 1958. Geophys Res Lett 36:3–7. doi: 10.1029/2008GL036076

Manney GL, Hegglin MI, Daffer WH, Santee ML, Ray EA, Pawson S, Schwartz MJ, Boone CD, Froidevaux L, Livesey NJ, Read WG, Walker KA (2011) Jet characterization in the upper troposphere/lower stratosphere (UTLS): Applications to climatology and transport studies. Atmos Chem Phys 11:6115–6137. doi: 10.5194/acp-11-6115-2011

McLandress C, Shepherd TG, Scinocca JF, Plummer DA, Sigmond M, Jonsson AI, Reader MC (2011) Separating the dynamical effects of climate change and ozone depletion. Part II: Southern Hemisphere troposphere. J Clim 24:1850–1868. doi: 10.1175/2010JCLI3958.1

Min S-K, Son S-W (2013) Multimodel attribution of the Southern Hemisphere Hadley cell widening: Major role of ozone depletion. J Geophys Res Atmos 118:3007–3015. doi: 10.1002/jgrd.50232

Ming Y, Ramaswamy V (2011) A model investigation of aerosol-induced changes in tropical circulation. J Clim 24:5125–5133. doi: 10.1175/2011JCLI4108.1

Molteni F, Stockdale TN, Vitart F (2015) Understanding and modelling extra-tropical teleconnections with the Indo-Pacific region during the northern winter. Climate Dyn. 45:3119-3140 doi: 10.1007/s00382-015-2528-y

Nakamura H, Sampe T, Tanimoto Y, Shimpo A (2004) Observed associations among storm tracks, jet streams and midlatitude oceanic fronts. Geophys Monogr 147:329–345

Pena-ortiz C, Gallego D, Ribera P, Ordonez P, Alvares-Castro MDC (2013) Observed trends in the global jet stream characteristics during the second half of the 20th century. J Geophys Res Atmos 118:2702–2713. doi: 10.1002/jgrd.50305

Pezza AB, Durrant T, Simmonds I, Smith I (2008) Southern Hemisphere synoptic behavior in extreme phases of SAM, ENSO, sea ice extent, and Southern Australia rainfall. J Clim 21:5566–5584. doi: 10.1175/2008JCLI2128.1

Pezza AB, Simmonds I, Renwick JA (2007) Southern hemisphere cyclones and anticyclones: recent trends and links with decadal variability in the Pacific Ocean. Int J Climatol 27:1403–1419. doi: 10.1002/joc.1477

Pezza AB, Rashid H a., Simmonds I (2012) Climate links and recent extremes in antarctic sea ice, high-latitude cyclones, Southern Annular Mode and ENSO. Clim Dyn 38:57–73. doi: 10.1007/s00382-011-1044-y

Polvani LM, Previdi M, Deser C (2011) Large cancellation, due to ozone recovery, of future Southern Hemisphere atmospheric circulation trends. Geophys Res Lett 38:1–6. doi: 10.1029/2011GL046712

Polvani LM, Waugh DW, Correa GJP, Son S-W (2011) Stratospheric Ozone Depletion: The Main Driver of Twentieth-Century Atmospheric Circulation Changes in the Southern Hemisphere. J Clim 24:795–812. doi: 10.1175/2010JCLI3772.1

Rayner NA, Parker DE, Horton EB, Folland CK, Alexander LV, Rowell DP, Kent EC, Kaplan A (2003) Global analyses of sea surface temperature, sea ice, and night marine air temperature since the late nineteenth century. J Geophys Res 108:4407-4443. doi:10.1029/2002JD002670

Rind D, Chandler M, Lerner J, Martinson DG, Yuan X (2001). Climate response to basin-specific changes in latitudinal temperature gradients and implications for sea ice variability. J Geophys Res 106:20161-20198. doi:10.1029/2000JD900643

Rudeva I, Simmonds I (2015) Variability and trends of global atmospheric frontal activity and links with large-scale modes of variability. J Clim 28:3311–3330. doi: 10.1175/JCLI-D-14-00458.1

Sampe T, Nakamura H, Goto A, Ohfuchi W (2010). Significance of a midlatitude SST frontal zone in the formation of a storm track and an eddy-driven westerly jet. J Clim, 23:1793–1814. doi:10.1175/2009JCLI3163.1

Seager R, Harnik N, Kushnir Y, Robinson W, Miller J (2003) Mechanisms of hemispherically symmetric climate variability*. J Clim 16:2960–2978. doi: 10.1175/1520-0442(2003)016<2960:MOHSCV>2.0.CO;2

Seidel D, Fu Q, Randel W, Reichler T (2008) Widening of the tropical belt in a changing climate. Nat Geosci 1:21–24. doi: 10.1038/ngeo.2007.38

Simmons AJ, Poli P, Dee DP, Berrisford P, Hersbach H, Kobayashi S, Peubey C (2014) Estimating low-frequency variability and trends in atmospheric temperature using ERA-Interim. Q J R Meteorol Soc 140:329–353. doi: 10.1002/qj.2317

Simmonds I (2015) Comparing and contrasting the behaviour of Arctic and Antarctic sea ice over the 35 year period 1979–2013. Ann Glaciol 56:18–28. doi: 10.3189/2015AoG69A909

Sinclair MR (1996) A climatology of anticyclones and blocking for the Southern Hemisphere. Mon Weather Rev 124:245–264

Strong C, Davis RE (2008) Variability in the position and strength of winter jet stream cores related to Northern Hemisphere teleconnections. J Clim 21:584–592. doi: 10.1175/2007JCLI1723.1

Son S-W, Tandon NF, Polvani LM, Waugh DW (2009) Ozone hole and Southern Hemisphere climate change. Geophys Res Lett 36:15075-15079. doi: 10.1029/2009GL038671

Son S-WW, Gerber EP, Perlwitz J, Polvani LM, Gillet NP, Seo K-H, Eyring V, Shepherd TG, Waugh D, Akiyoshi H, Austin J, Baumgaertner A, Bekki S, Braesicke P, Brühl C, Butchart N, Chipperfield MP, Cugnet D, Dameris M, Dhomse S, Frith S, Garny H, Garcia R, Hardiman SC, Jöckel P, Lamarque JF, Mancini E, Marchand M, Michou M, Nakamura T, Morgenstern O, Pitari G, Plummer DA, Pyle J, Rozanov E, Scinocca JF, Shibata K, Smale D, Teyssedre H, Tian W, Yamashita Y (2010) Impact of stratospheric ozone on Southern Hemisphere circulation change: A multimodel assessment. J Geophys Res 115:1–18. doi: 10.1029/2010JD014271

Thompson DWJ, Solomon S (2002) Interpretation of recent Southern Hemisphere climate change. Science 296:895–899. doi: 10.1126/science.1069270

Trenberth KE (1997). The definition of El Niño. Bull Am Meteorol Soc 78:2771–2777. doi:10.1175/15200477 (1997) 078<2771: TDOENO>2.0. CO;2

Turner J (2004) The El Niño–southern oscillation and Antarctica. Int J Climatol 24:1–31. doi: 10.1002/joc.965

Watterson IG (2015) Improved simulation of regional climate by global models with higher resolution: Skill scores correlated with grid length*. J Clim 28:5985–6000. doi: 10.1175/JCLI-D-14-00702.1

Wenzel S, Eyring V, Gerber EP, Karpechko AY (2016) Constraining Future Summer Austral Jet Stream Positions in the CMIP5 Ensemble by Process-Oriented Multiple Diagnostic Regression. J Clim 29:673-687. doi: http://dx.doi.org/10.1175/JCLI-D-15-0412.1

Vuuren DP van, Edmonds J, Kainuma M, Riahi K, Thomson A, Hibbard K, Hurtt GC, Kram T, Krey V, Lamarque J-F, Masui T, Meinshausen M, Nakicenovic N, Smith SJ, Rose SK (2011) The representative concentration pathways: an overview. Clim Change 109:5–31. doi: 10.1007/s10584-011-0148-z

Yuan, X. (2004). ENSO-related impacts on Antarctic sea ice: a synthesis of phenomenon and mechanisms. Antarct Sci 16:415–425. doi:10.1017/S0954102004002238

Zhang L, Wu L, Yu L (2011) Oceanic origin of a recent La Niña-like trend in the tropical Pacific. Adv Atmos Sci 28:1109–1117. doi: 10.1007/s00376-010-0129-6

Zhang Y, Wallace J, Battisti D (1997) ENSO-like interdecadal variability: 1900-93. J Clim 10:1004–1020.

FIGURE CAPTIONS

Figure 1 A meridional cross section over 240 – 260° E showing Hadley cell represented by the streamlines (in red), the mean zonal wind speed (black contours, ms-1) and temperature (shaded,°C) for July 1997. The box shows the poleward edge of the Hadley Circulation which coincides with the location of STJ.

Figure 2 Map of Southern Hemisphere with the box showing the area of the study.

Figure 3 Monthly mean of (a) zonal wind strength of the STJ and (b) meridional location of the STJ from ERA-Interim (1979 – 2012). The whiskers indicate one standard deviation and the circles indicate the range of the values.

Figure 4 Seasonal average of zonal wind speed (ms^{-1}) for 1979 - 2012 with a contour interval of 5 ms^{-1} at 300hPa-100hPa.

Figure 5 Mean winter zonal wind speed during El Niño and La Niña years (a) and (c) and the standardised anomalies (b) and (d) at 300hPa-100hPa from ERA Interim.

Figure 6 Standardised anomalies of zonal wind speed for all the El Niño years from 1979 to 2012 from CMIP5 models at 300-100 hPa.

Figure 7 Standardised anomalies of zonal wind speed for all the La Niña years from 1979 to 2012 from CMIP5 models at 300-100 hPa.

Figure 8 Anomaly correlation coefficient of zonal wind for all the El Niño events during JJA from 1979 to 2012 from CMIP5 models with ERA Interim at 300-100 hPa.

Figure 9 Anomaly correlation coefficient of zonal wind for all the La Niña events during JJA from 1979 to 2012 from CMIP5 models with ERA Interim at 300-100 hPa.

Figure 10 Anomaly correlation coefficient of zonal wind between the CMIP5 models and ERA-Interim a) during El Niño events and b) during La Niña events from the area of study at 300-100 hPa. The whiskers in the graph show 95% confidence interval for the respective models.

Figure 11 (a) Mean winter jet strength trend in the historical simulation (1979 - 2012), sorted by magnitude. The dash vertical line and the dot-dash lines in the figure represent the trend in the jet strength in ERA-Interim and position of zero respectively. The blue coloured data points show models that have statistically significant trends in the strength at the 5% significant level using two-tailed student test.

Figure 11 (b) Multi-model mean of the STJ strength from the CMIP5 models and ERA-Interim.

Figure 12 (a) The trend in the winter zonal wind speed at 300-100 hPa for 1979 – 2012 from ERA-Interim. (The box shows the study area).

Figure 12 (b) The trend in the winter zonal wind speed at 300-100 hPa for 1979 – 2012 from the multi-model mean. (The box shows the study area).

Figure 13 (a) Winter SST trend for 1979-2012 from HadISST.

Figure 13 (b) The multi-model mean winter SST trend for 1979-2012.

Figure 14 The correlation between the mean winter SST from HadISST for the Niño 3.4 area and the mean winter STJ strength from ERA-Interim.

Figure 15 (a) Mean meridional location of the STJ and (b) Trend in the meridional location of STJ in the historical CMIP5 simulations and ERA in the study area. The dash vertical line and the dot-dash lines in the figure represent ERA-Interim and position of zero respectively.

Figure 15 (b)The ERA-Interim and CMIP5 multi-model mean trends in the meridional location of the STJ.

Figure 16 The ERA-Interim and CMIP5 multi-model mean trends in the meridional location of the STJ.

Figure 17 The trends in the strength of the STJ for (a) RCP 4.5 and RCP 8.5 (b) projections for 2011-2099 sorted by magnitude. The blue coloured data points show models that have statistically significant trends in the strength at the 5% significant level using two-tailed student test.

Figure 18 The multi-model mean of the winter STJ strength over 2011-2099 for RCP 4.5 and RCP 8.5.

Figure 19 Trends in the meridional location of STJ for (a) RCP 4.5 and (b) RCP 8.5 sorted by magnitude. The dot-dash line in the figure represents the position of zero. The blue coloured data points show models that have statistically significant trends in the meridional location at the 5% significant level using two-tailed student test.

Figure 20 The multi-model mean winter meridional location of the STJ 2011-2099 for RCP 4.5 and RCP 8.5.

Figure 21 Spatial correlations between the multi-model mean projected trend in jet strength (2011-2099) and the multi-model mean projected SST trend from (a) RCP 4.5 and (b) RCP 8.5 scenarios.

Figure 22 Projected SST trends from RCP 4.5 (a) IPSL-CM5A-LR (b) INMCM4 (d) CISRO-Mk3.6.0 (d) MIROC-ESM-CHEM for 2011-2099.

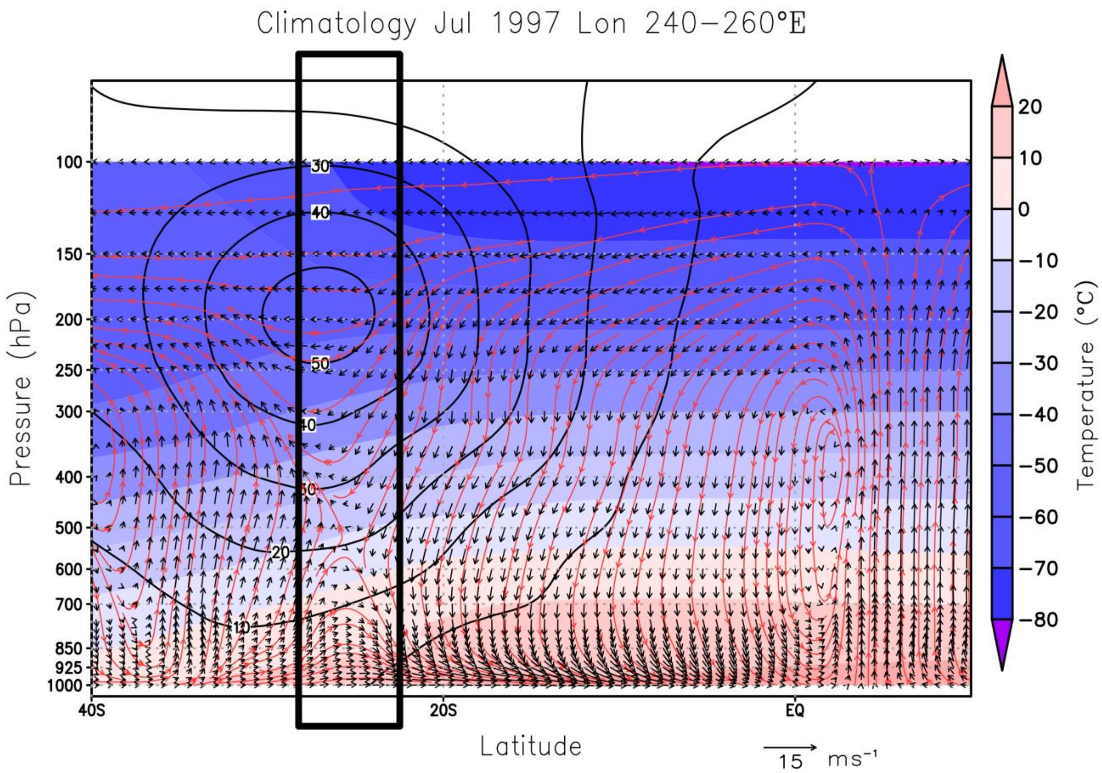

Figure 1 Hadley Circulation (black arrows, ms^{-1}) averaged between 240°E and 260°E with streamlines (red in clour), the mean zonal wind speed (black contours, ms^{-1}) and temperature (shaded,°C) for July 1997. The box shows the poleward edge of Hadley Circulation which coincides with the location of STJ.

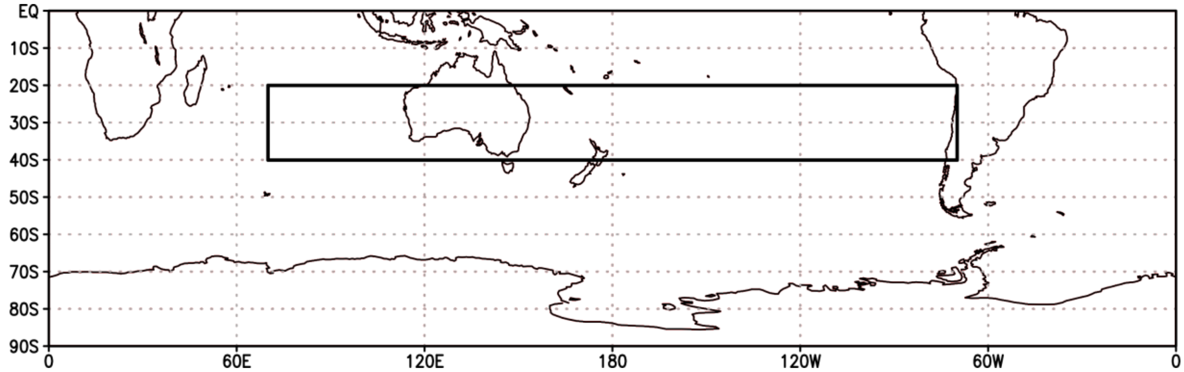

Figure 2 Map of Southern Hemisphere with the box showing the area of the study.

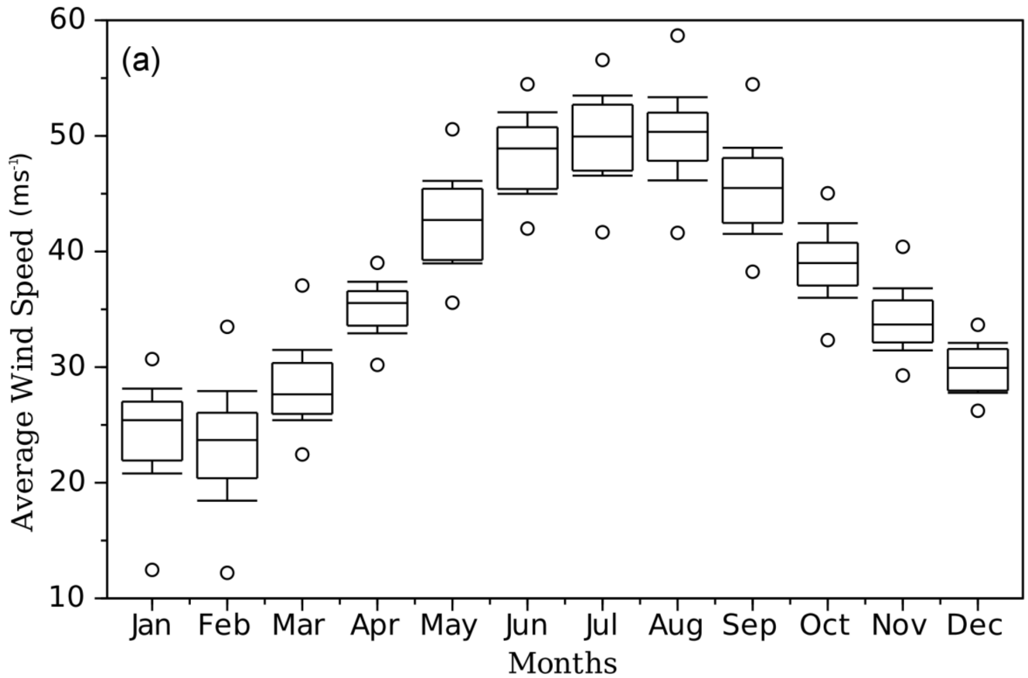

Figure 3 (a)

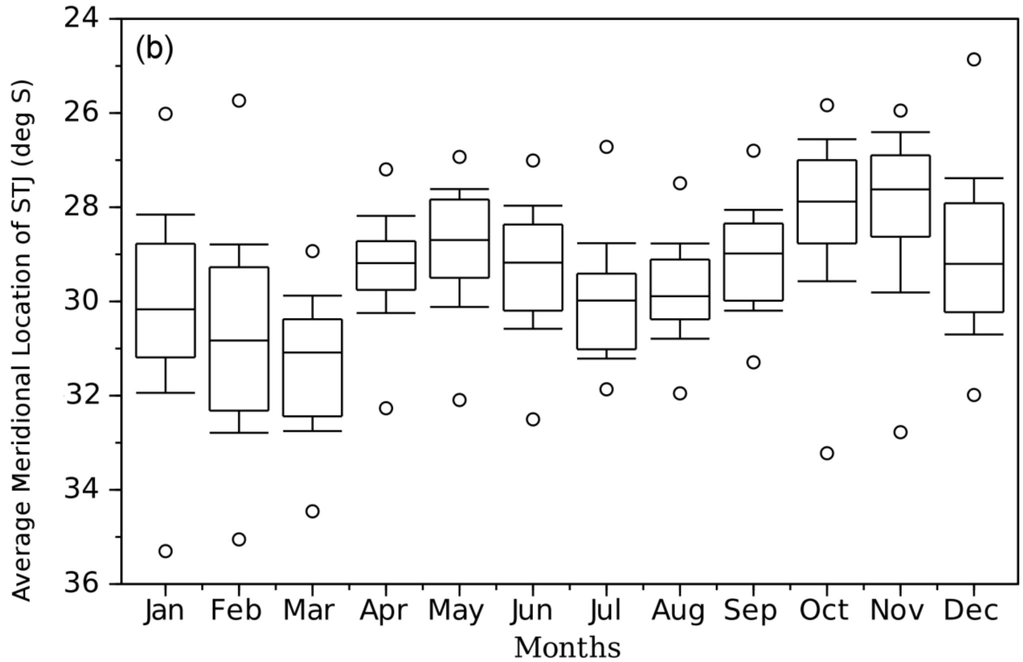

Figure 3 (b)

Figure 3 Monthly mean of (a) zonal wind strength of the STJ and (b) meridional location of the STJ from ERA-Interim (1979 – 2012). The whiskers indicate one standard deviation and the circles indicate the range of the values.

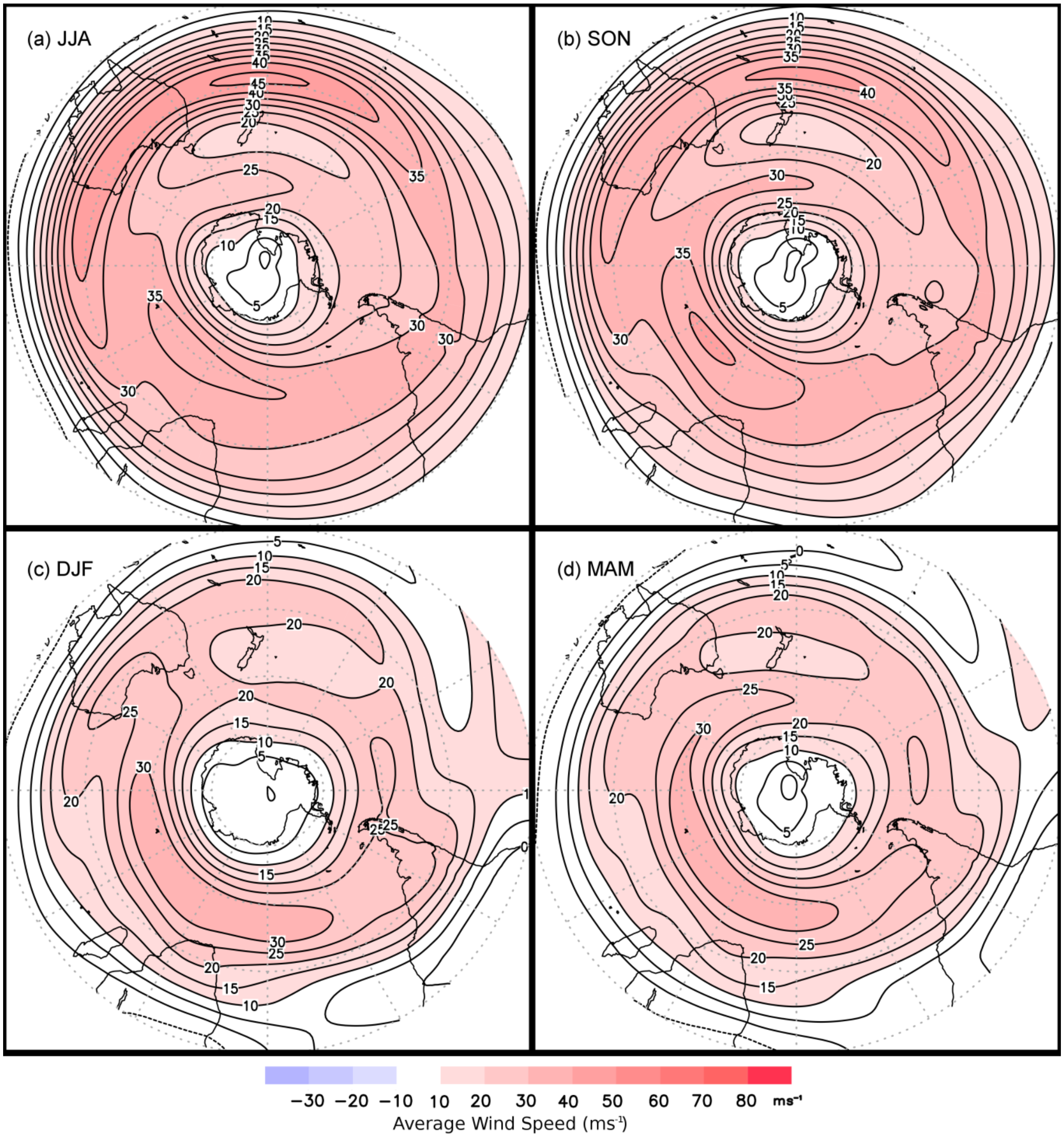

Figure 4 Seasonal average of zonal wind speed (ms^{-1}) for 1979 - 2012 with a contour interval of 5 ms^{-1} at 300hPa-100hPa.

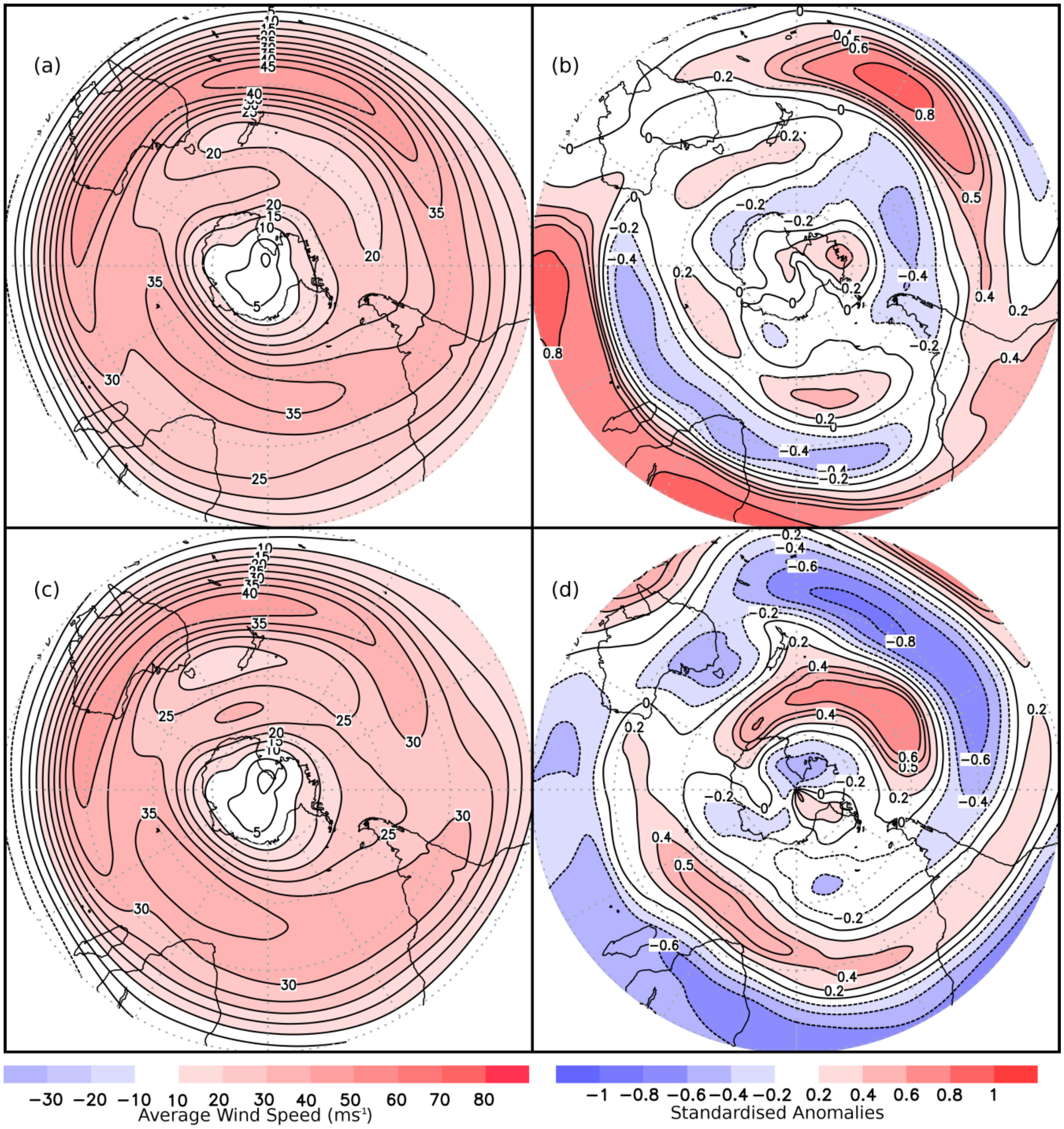

Figure 5 Mean winter zonal wind speed during El Niño and La Niña years (a) and (c) and the standardised anomalies (b) and (d) at 300hPa-100hPa.

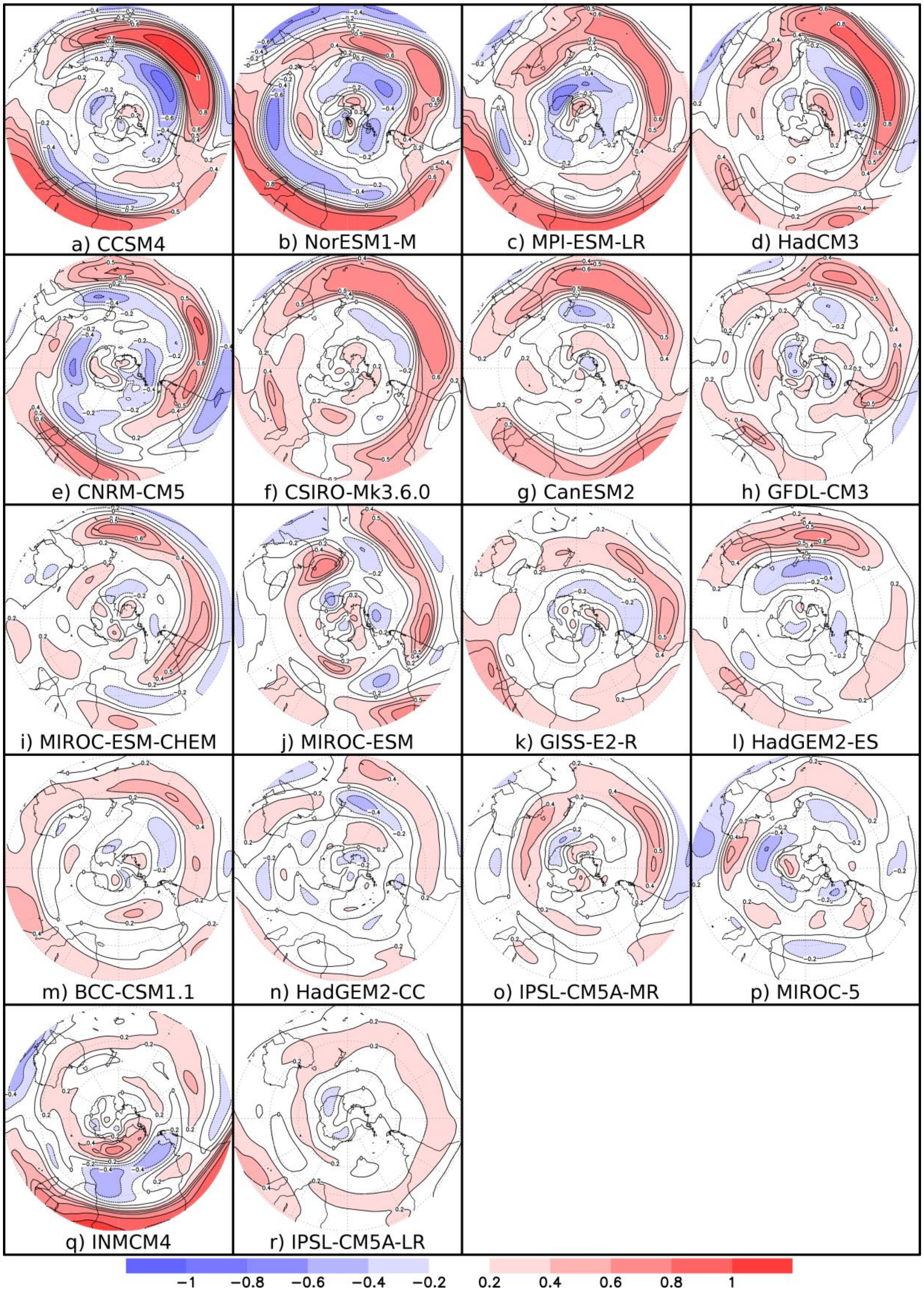

Figure 6 Standardised anomalies of zonal wind speed for all the El Niño years from 1979 to 2012 from CMIP5 models at 300-100 hPa.

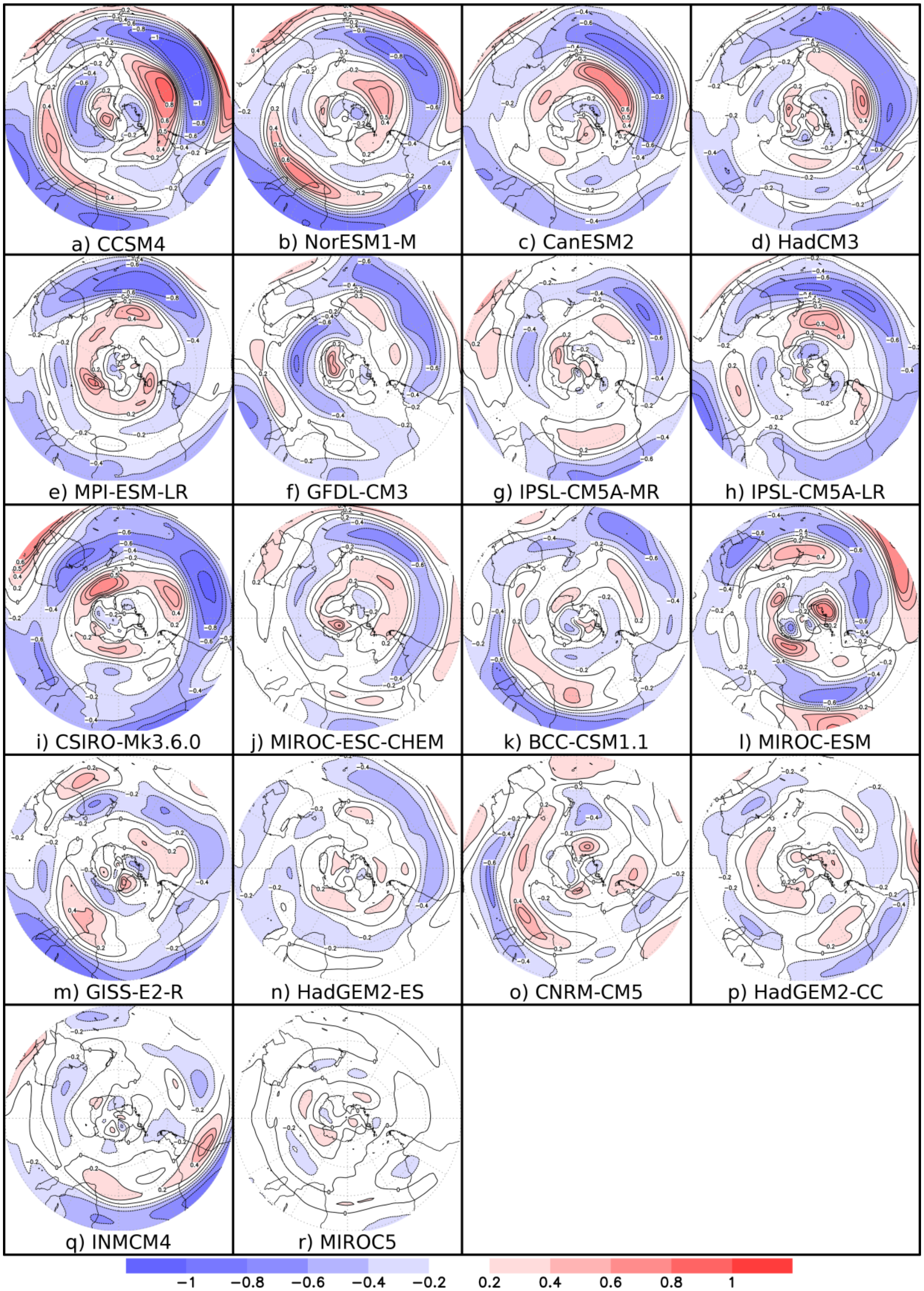

Figure 7 Standardised anomalies of zonal wind speed for all the La Niña years from 1979 to 2012 from CMIP5 models at 300-100 hPa.

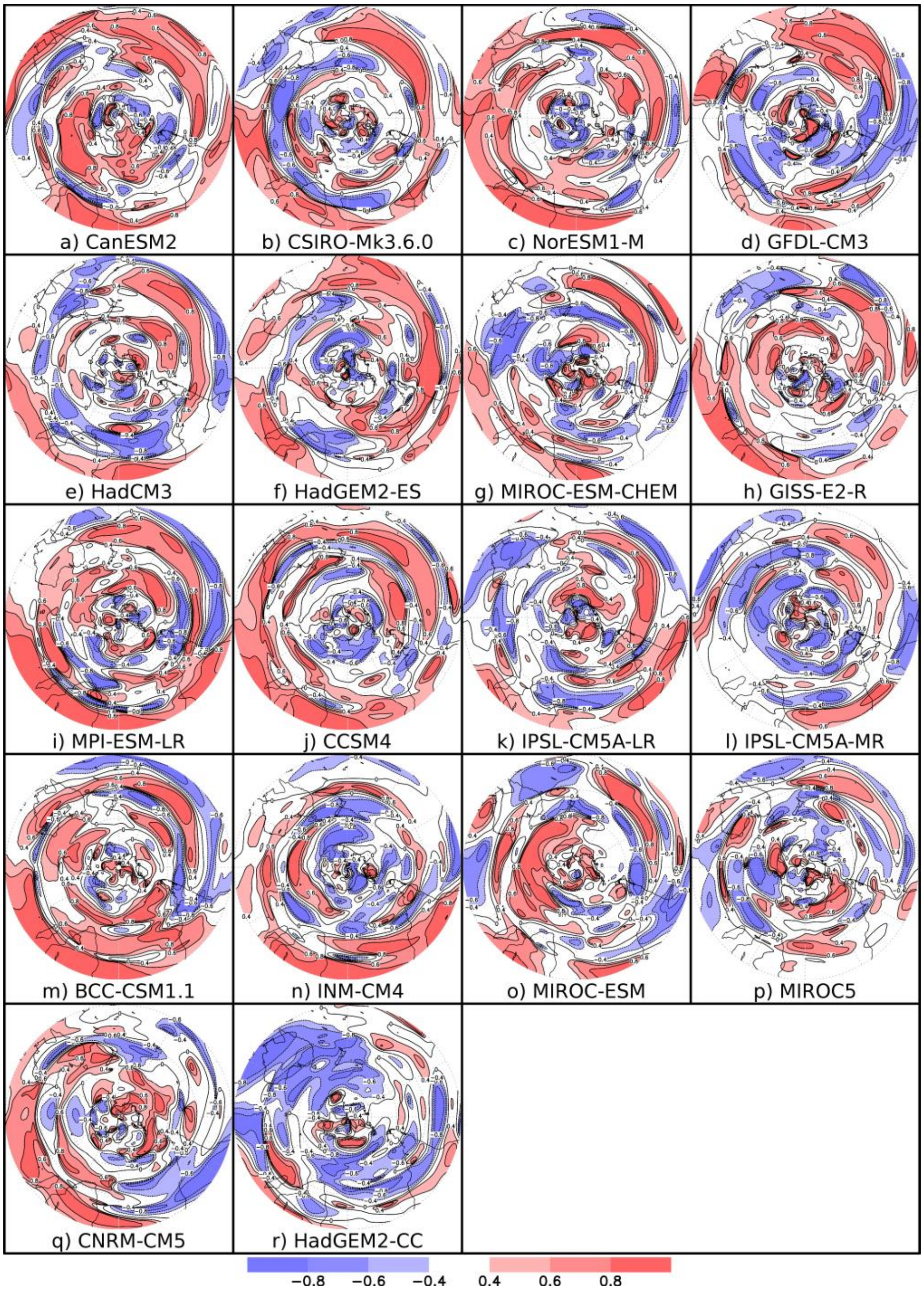

Figure 8 Anomaly correlation coefficient of zonal wind for all the El Niño events during JJA from 1979 to 2012 from CMIP5 models with ERA Interim at 300-100 hPa.

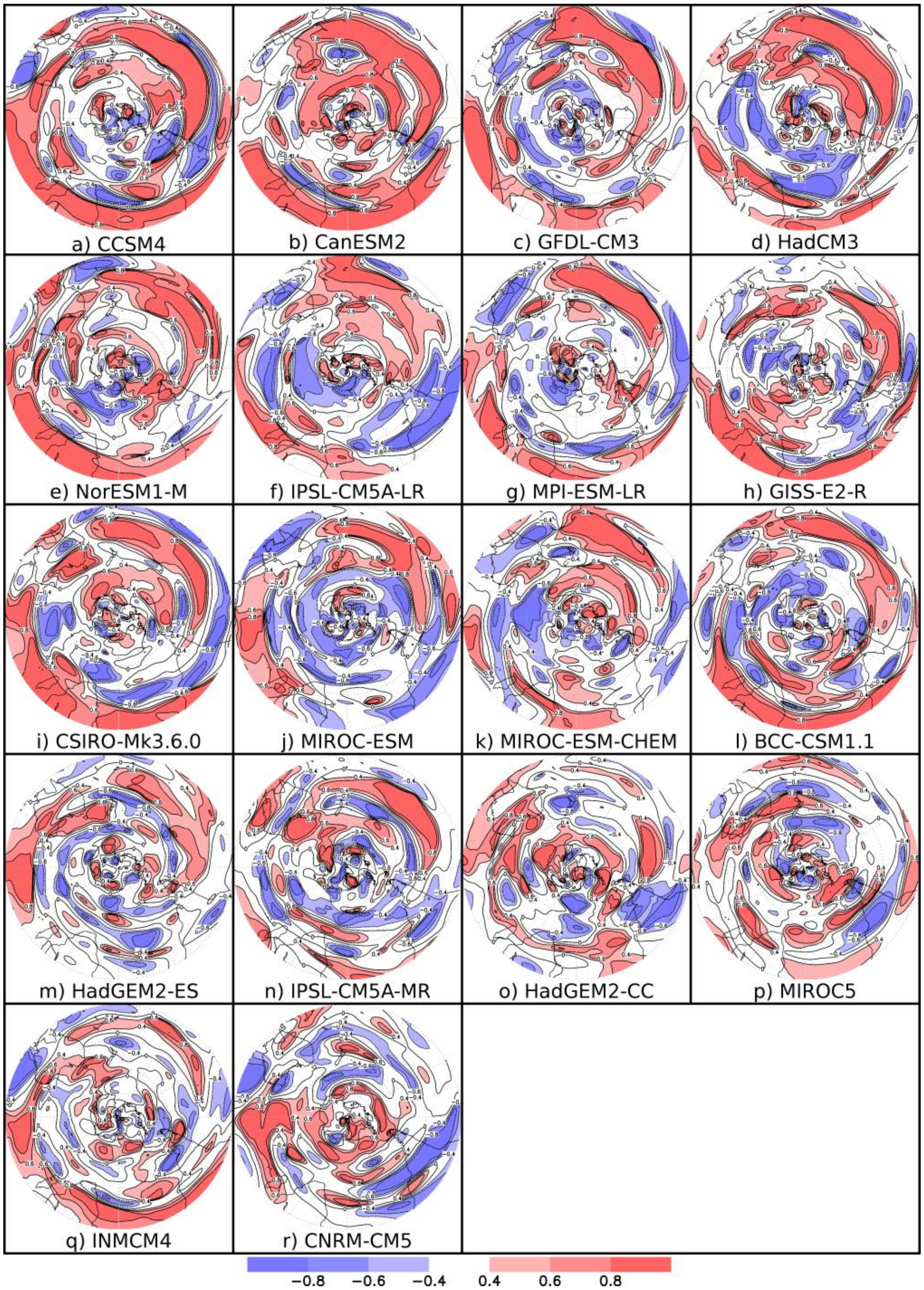

Figure 9 Anomaly correlation coefficient of zonal wind for all the La Niña events during JJA from 1979 to 2012 from CMIP5 models with ERA Interim at 300-100 hPa.

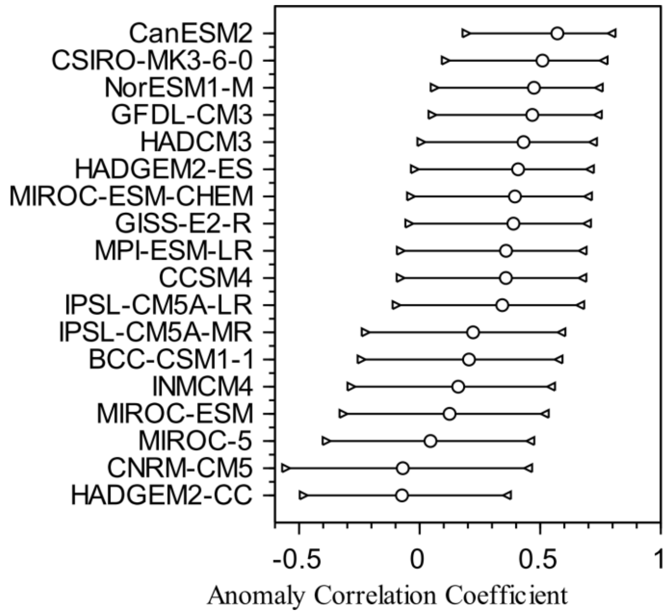

Figure 10 (a)

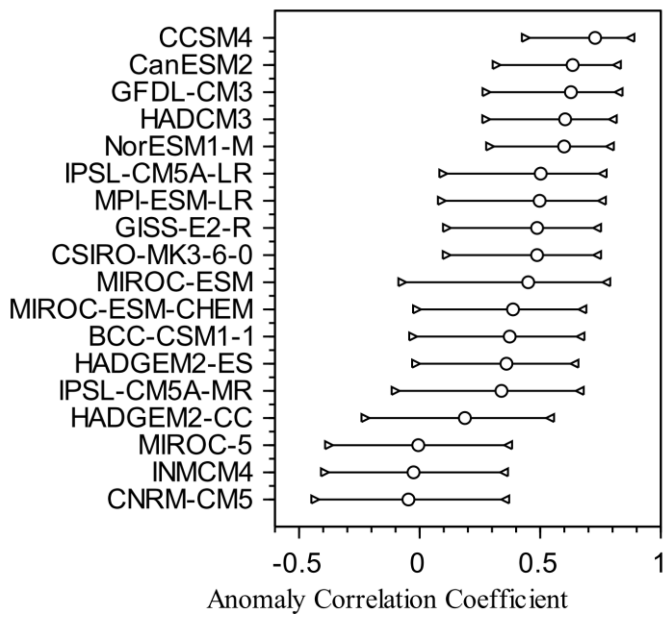

Figure 10 (b)

Figure 10 Anomaly correlation coefficient of zonal wind between the CMIP5 models and ERA-Interim a) during El Niño events and b) during La Niña events from the area of study at 300-100 hPa. The whiskers in the graph show 95% confidence interval for the respective models.

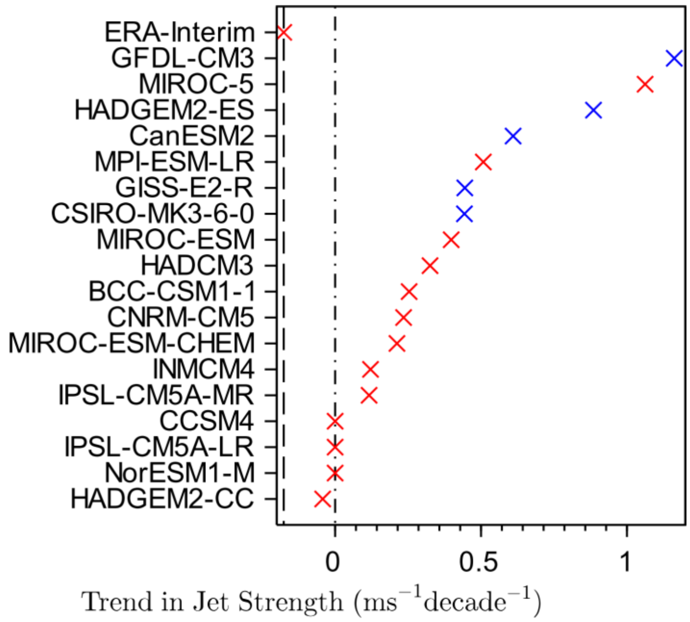

Figure 11 (a) Mean winter jet strength trend in the historical simulation (1979 - 2012), sorted by magnitude. The dash vertical line and the dot-dash lines in the figure represent the trend in the jet strength in ERA-Interim and position of zero respectively. The blue coloured data points show models that have statistically significant trends in the strength at the 5% significant level using two-tailed student test.

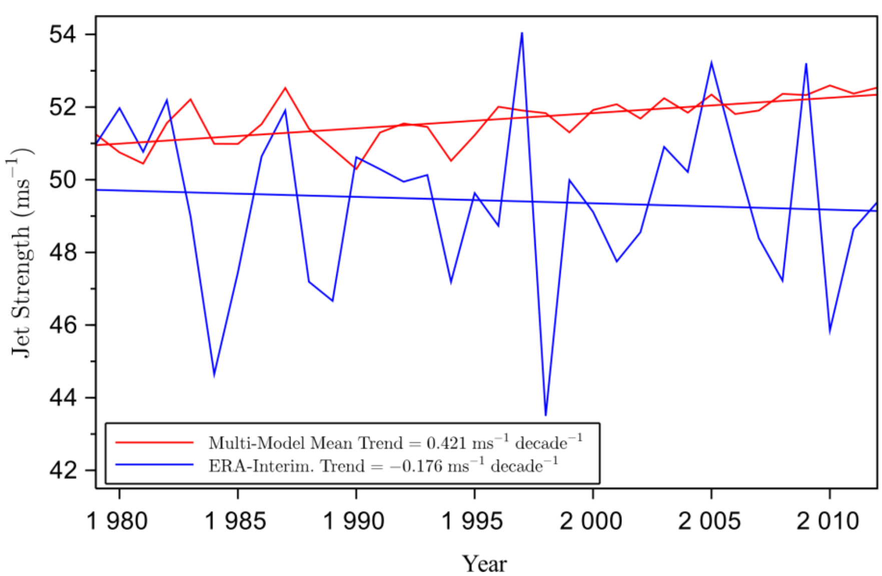

Figure 11 (b) Multi-model mean of the STJ strength from the CMIP5 models and ERA-Interim.

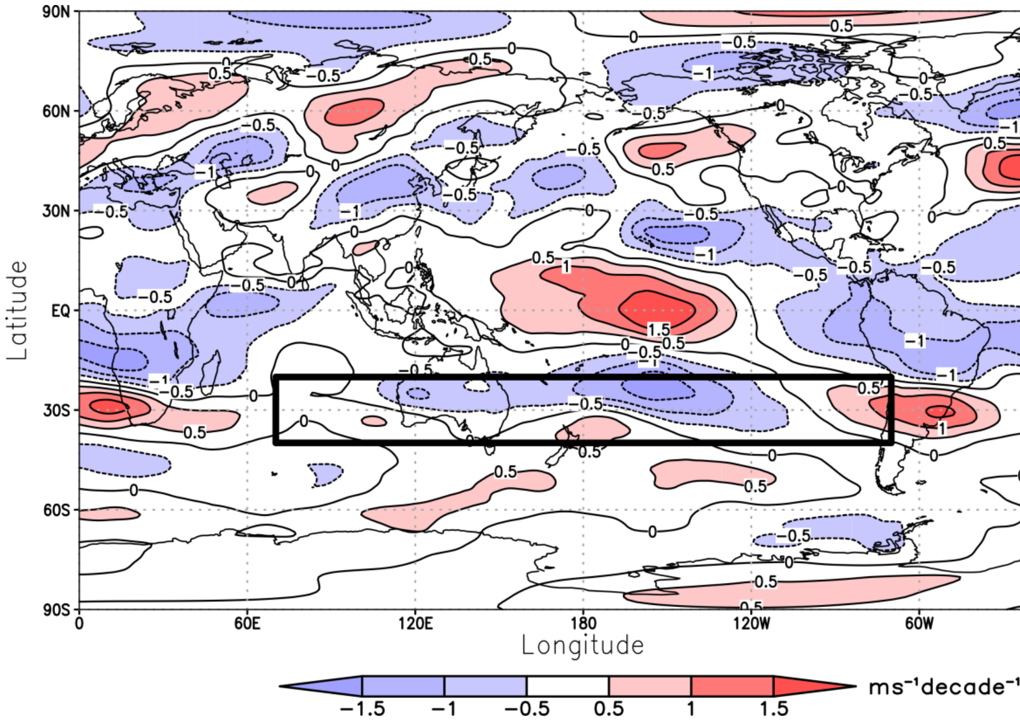

Figure 12 (a) The trend in the winter zonal wind speed at 300-100 hPa for 1979 – 2012 from ERA-Interim. (The box shows the study area).

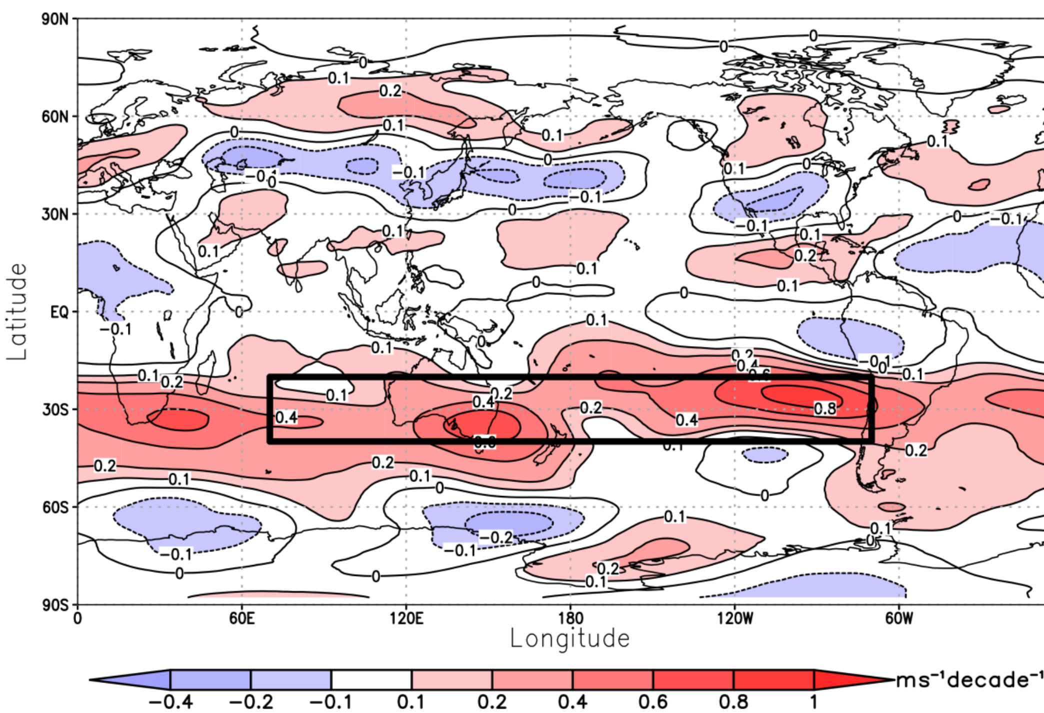

Figure 12 (b) The trend in the winter zonal wind speed at 300-100 hPa for 1979 – 2012 from the multi-model mean. (The box shows the study area).

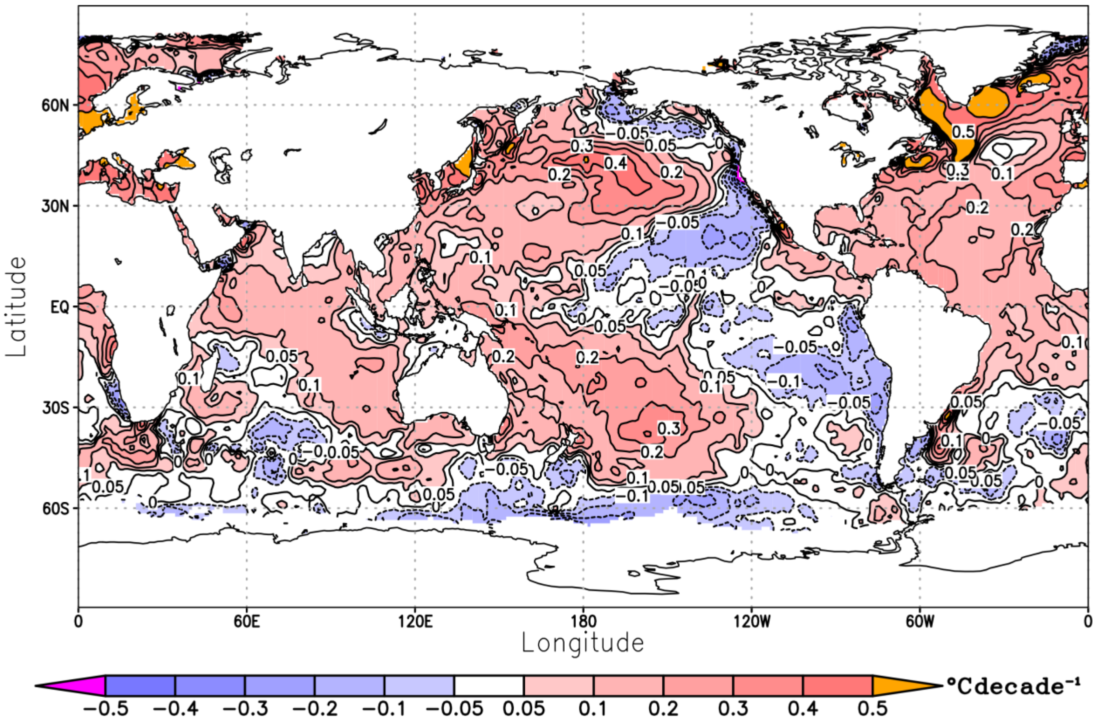

Figure 13 (a) Winter SST trend for 1979-2012 from HadISST.

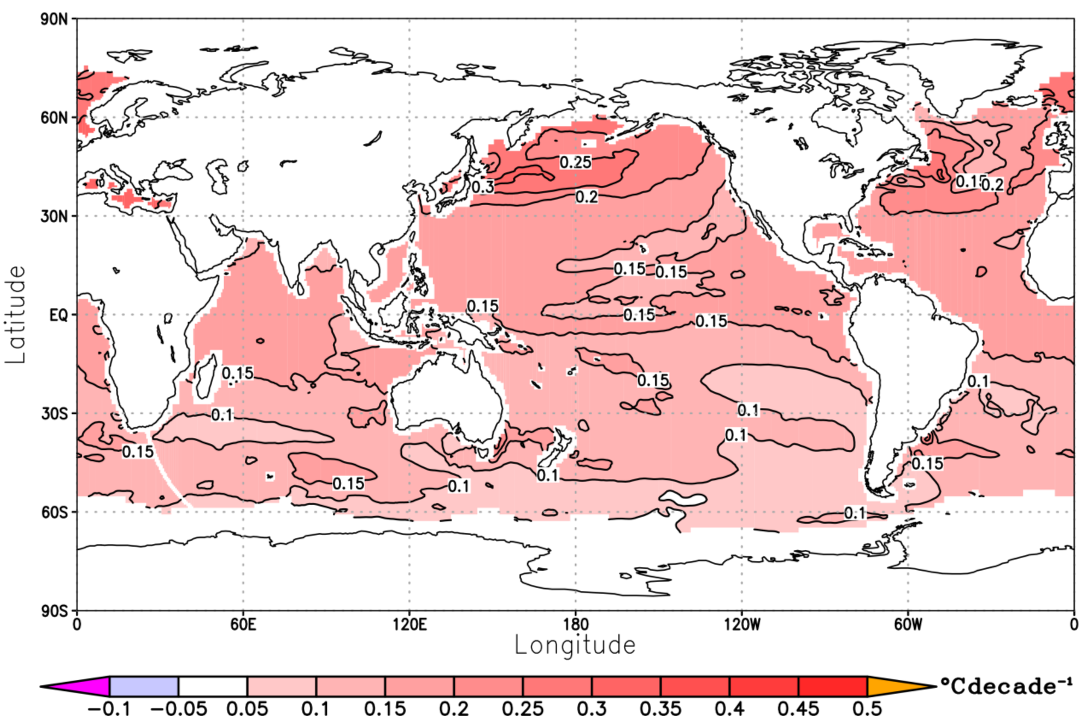

Figure 13 (b) The multi-model mean winter SST trend for 1979-2012.

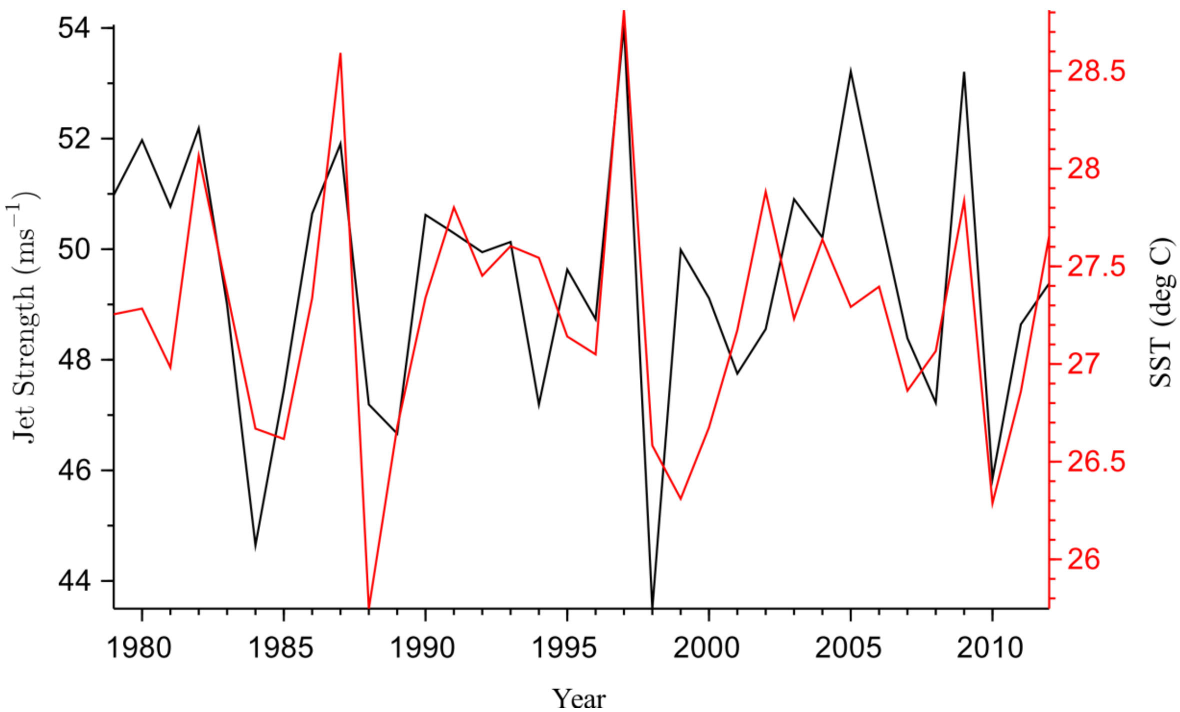

Figure 14 The correlation between the mean winter SST from HadISST for the Niño 3.4 area and the mean winter STJ strength from ERA-Interim.

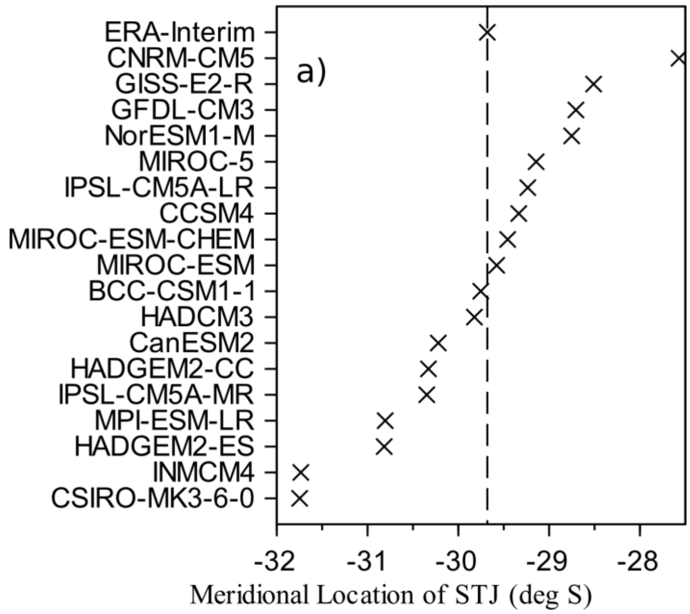

Figure 15 (a)

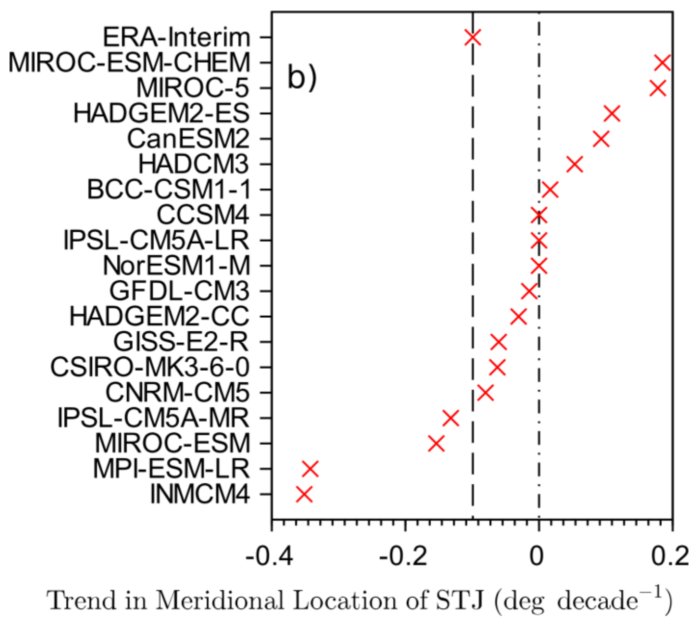

Figure 15 (b)

Figure 15 (a) Mean meridional location of the STJ and (b) Trend in the meridional location of STJ in the historical CMIP5 simulations and ERA in the study area. The dash vertical line and the dot-dash lines in the figure represent ERA-Interim and position of zero respectively.

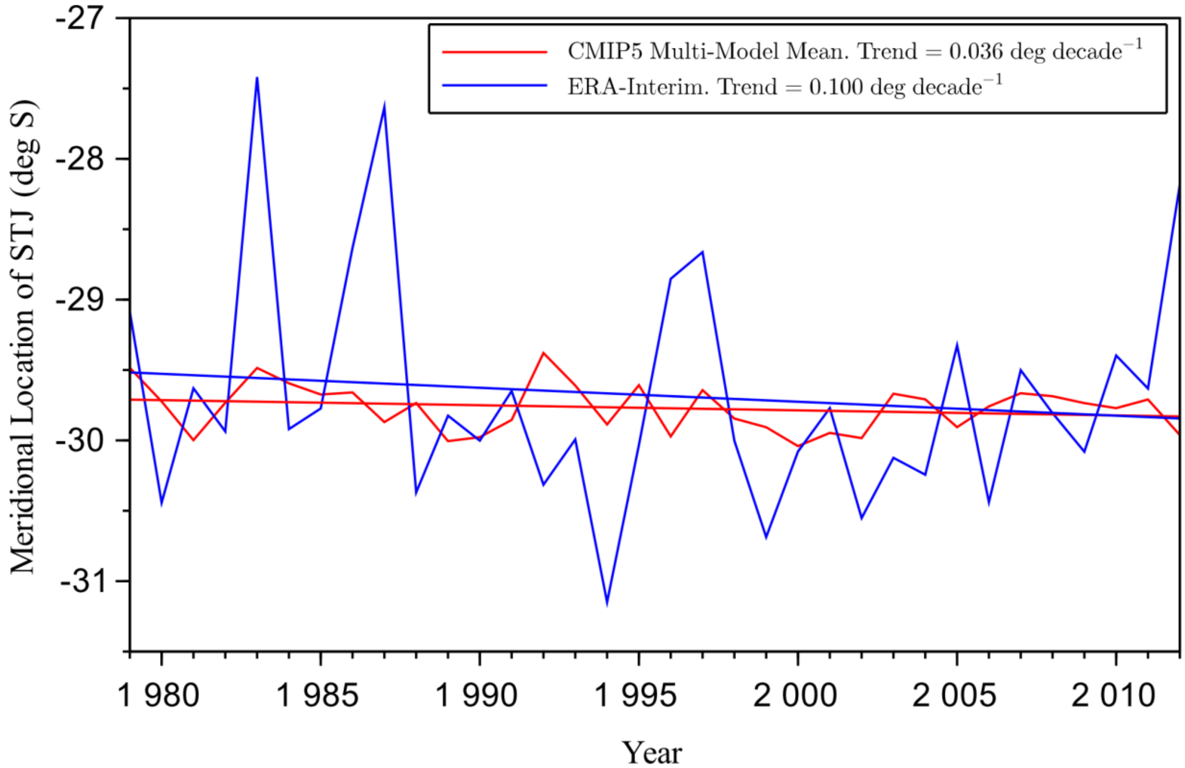

Figure 16 The ERA-Interim and CMIP5 multi-model mean trends in the meridional location of the STJ.

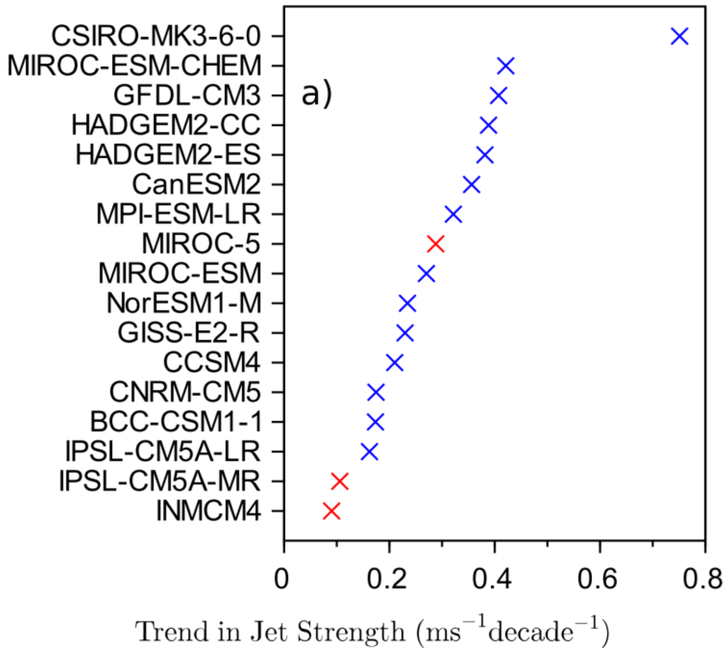

Figure 17 (a)

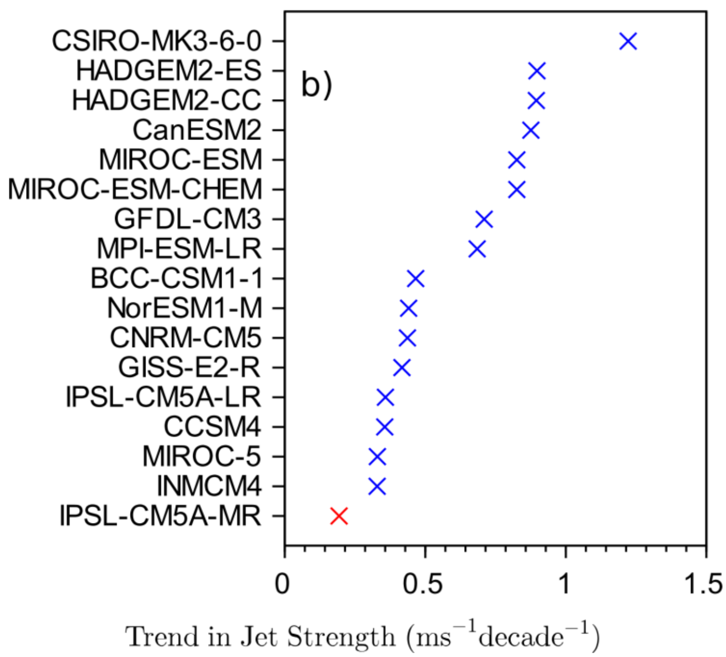

Figure 17 (b)

Figure 17 The trends in the strength of the STJ for (a) RCP 4.5 and RCP 8.5 (b) projections for 2011-2099 sorted by magnitude. The blue coloured data points show models that have statistically significant trends in the strength at the 5% significant level using two-tailed student test.

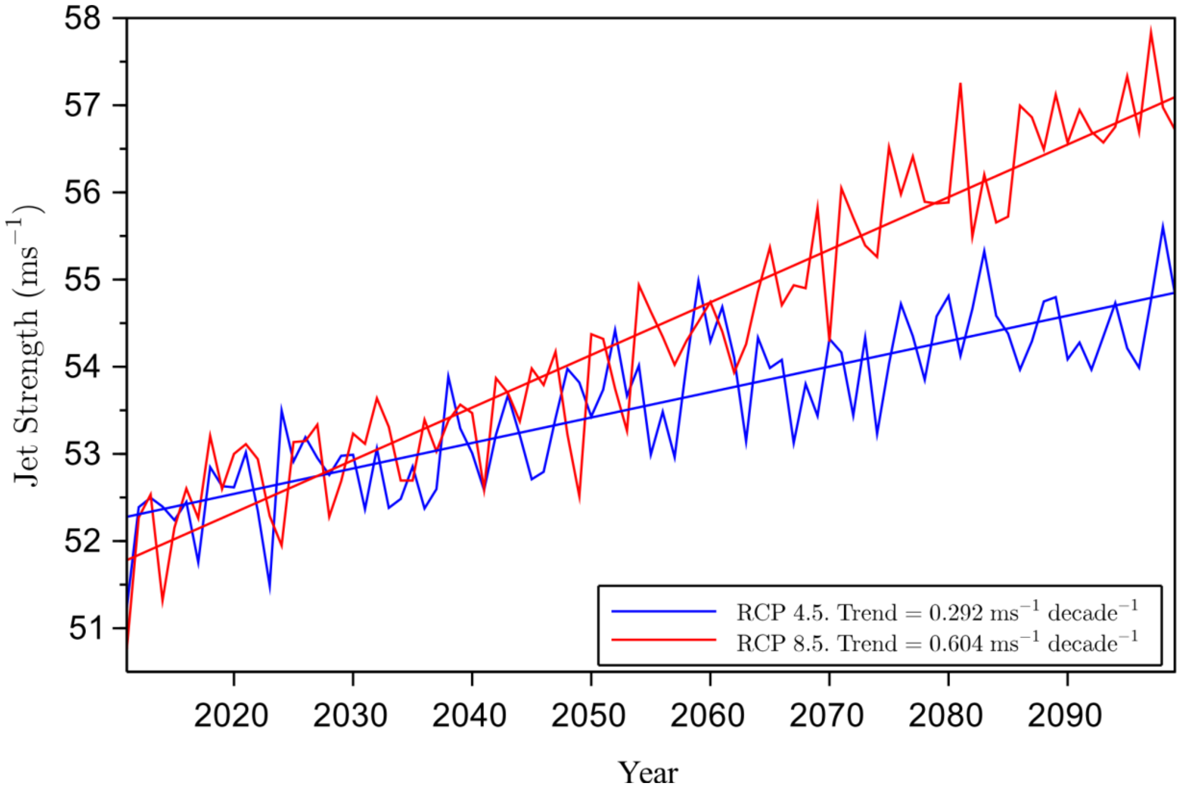

Figure 18 The multi-model mean of the winter STJ strength over 2011-2099 for RCP 4.5 and RCP 8.5.

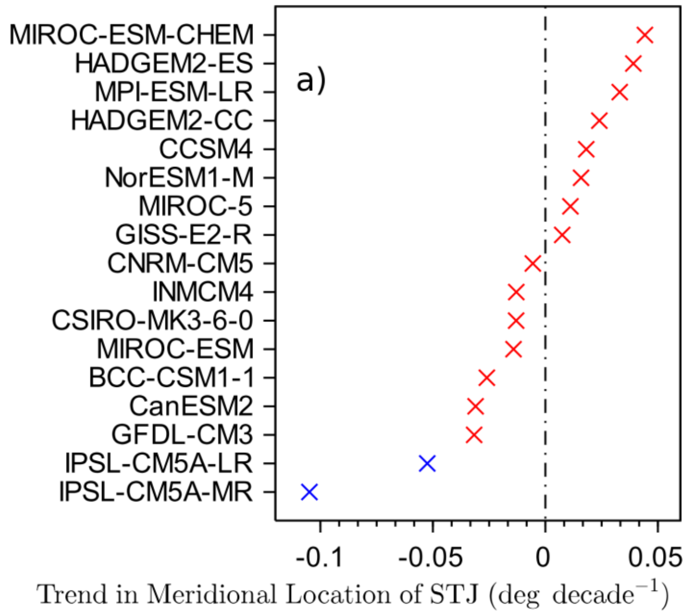

Figure 19 (a)

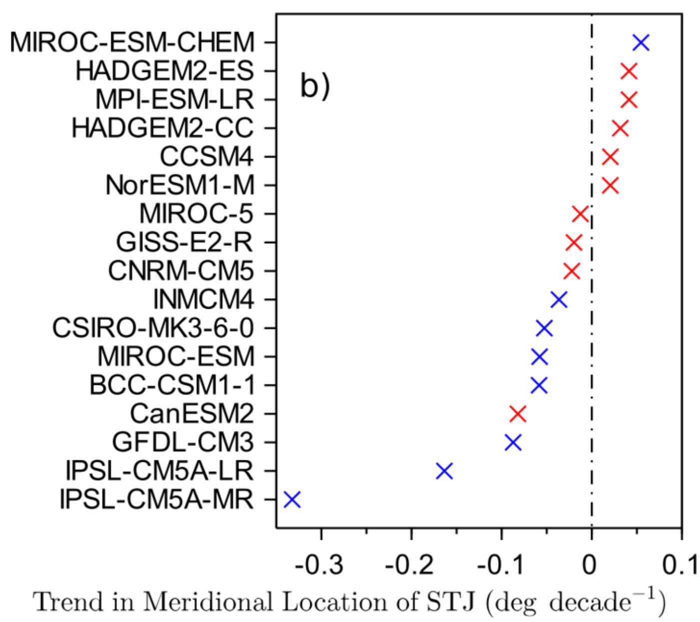

Figure 19 (b)

Figure 19 Trends in the meridional location of STJ for (a) RCP 4.5 and (b) RCP 8.5 sorted by magnitude. The dot-dash line in the figure represents the position of zero. The blue coloured data points show models that have statistically significant trends in the meridional location at the 5% significant level using two-tailed student test.

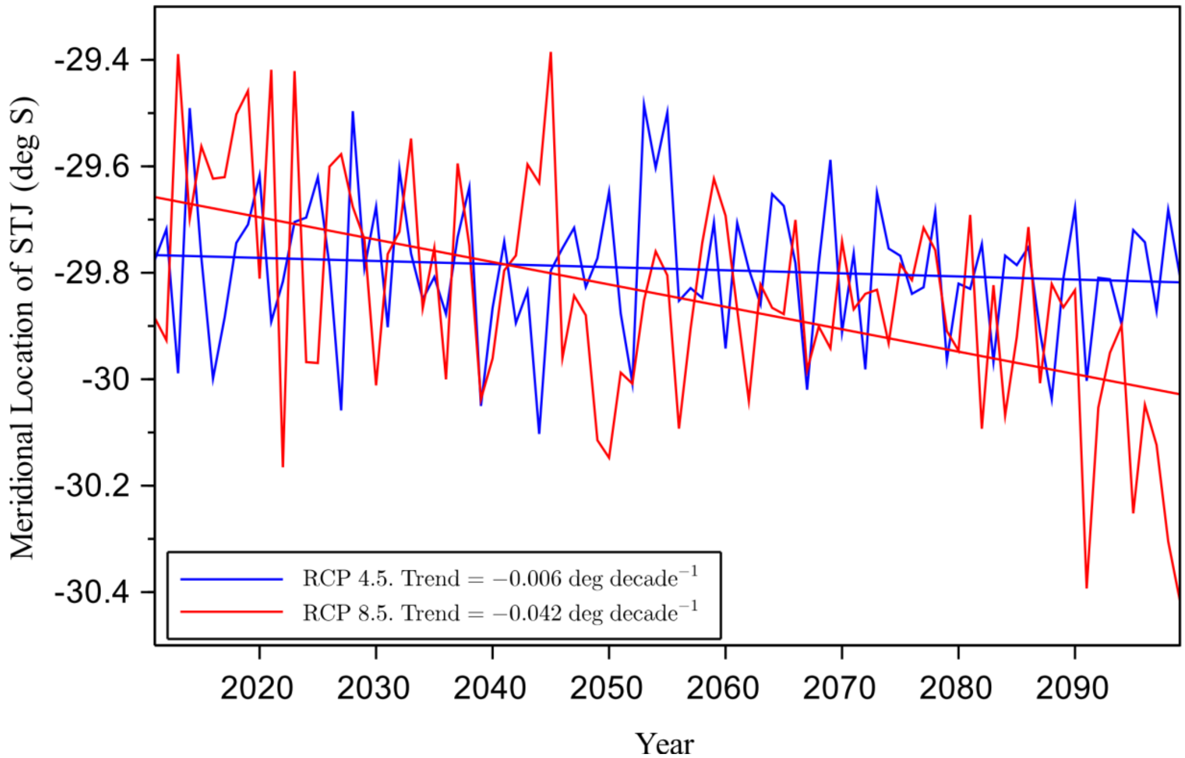

Figure 20 The multi-model mean winter meridional location of the STJ 2011-2099 for RCP 4.5 and RCP 8.5.

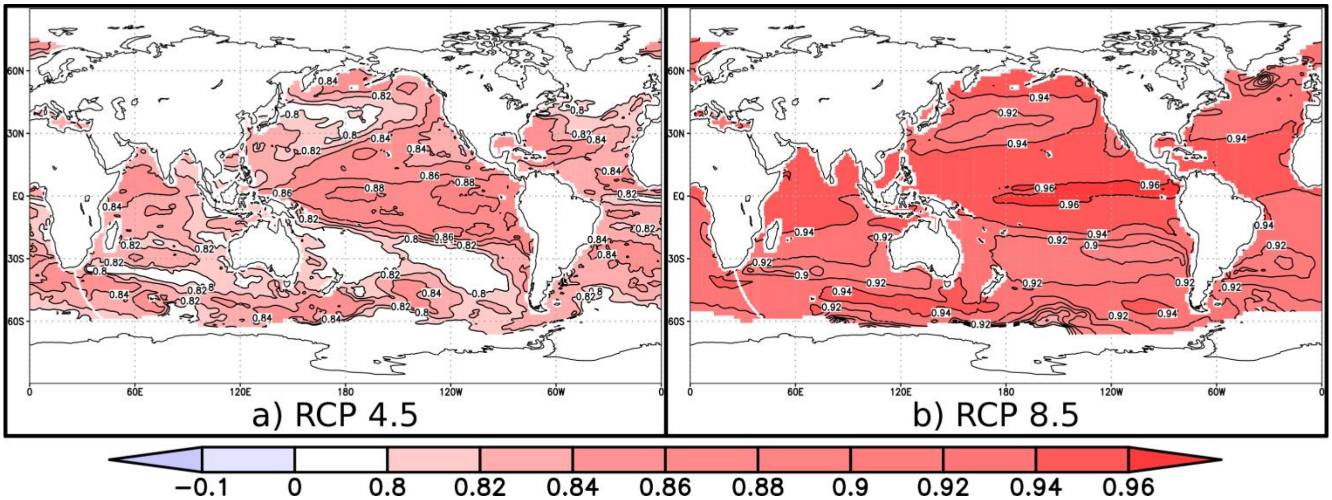

Figure 21 Spatial correlations between the multi-model mean projected trend in jet strength (2011-2099) and the multi-model mean projected SST trend from (a) RCP 4.5 and (b) RCP 8.5 scenarios.

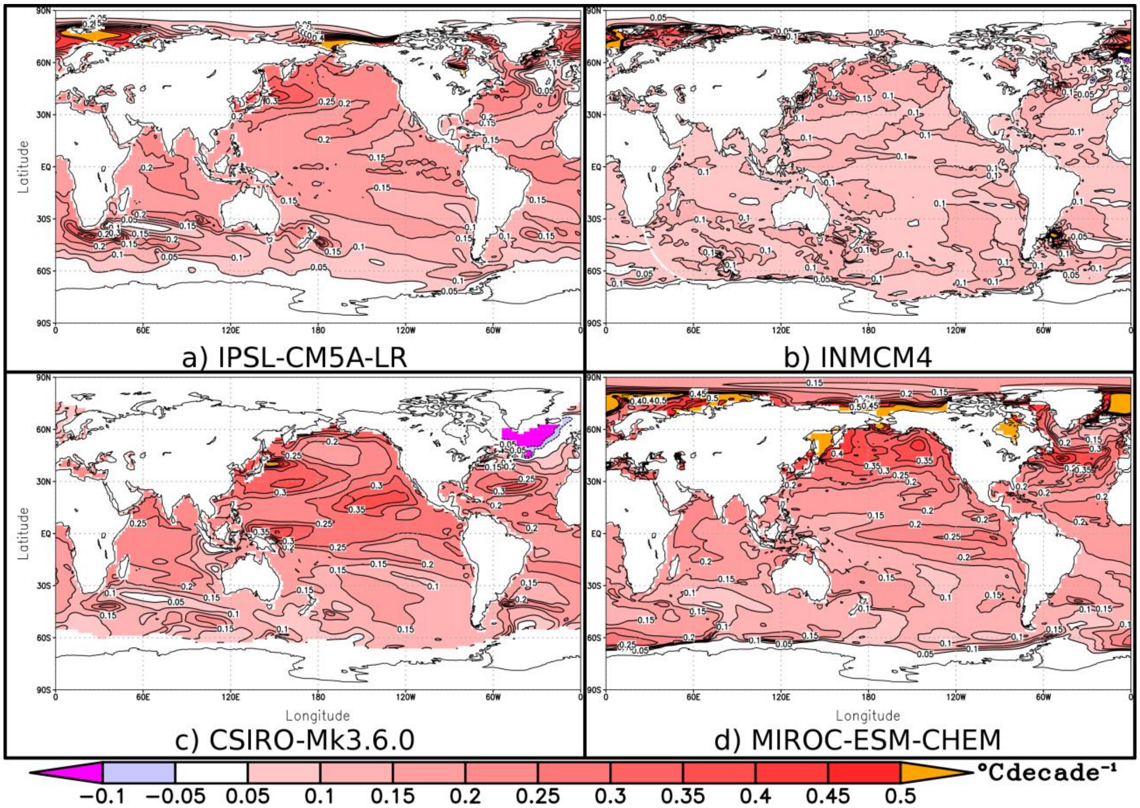

Figure 22 Projected SST trends from RCP 4.5 (a) IPSL-CM5A-LR (b) INMCM4 (d) CISRO-Mk3.6.0 (d) MIROC-ESM-CHEM for 2011-2099.

Table 1 CMIP5 models used in this study, indicating the country of origin and the resolution.

Model	Country	Resolution (longitude × latitude)	Number of El Niño years/La Niña years
BCC-CSM1.1	China	2.8125° × 2.767°	11/8
CanESM2	Canada	2.8125° × 2.767°	11/6
CCSM4	USA	1.25° × 0.9424°	8/7
CNRM-CM5	France	1.40625°× 1.40625°	5/8
CSIRO-Mk3.6.0	Australia	2.875° × 1.849°	11/8
GFDL-CM3	USA	2.0° × 2.5°	11/7
GISS-E2-R	USA	2.5° × 2.0°	13/8
HadCM3	UK	3.75° × 2.5°	11/8
HadGEM2-CC	UK	1.875° × 1.25°	9/8
HadGEM2-ES	UK	1.875° × 1.25°	9/9
INM-CM4	Russia	2.0° × 1.5°	8/10
IPSL-CM5A-LR	France	3.75° × 3.7895°	11/7
IPSL-CM5A-MR	France	2.5° × 1.2676°	11/7
MIROC5	Japan	1.40625° × 1.389°	8/13
MIROC-ESM	Japan	2.8125° × 2.767°	7/5
MIROC-ESM-CHEM	Japan	2.8125° × 2.767°	8/8
MPI-ESM-LR	Germany	1.875 ° × 2.767°	9/7
NorESM1-M	Norway	2.5° × 1.89745°	8/9